

## The Central 300 pc of the Galaxy probed by infrared spectra of H<sub>3</sub><sup>+</sup> and CO: II. Expansion and morphology of the warm diffuse gas

TAKESHI OKA<sup>1</sup> AND T. R. GEBALLE<sup>2</sup>

<sup>1</sup>*Department of Astronomy and Astrophysics and Department of Chemistry, the Enrico Fermi Institute, University of Chicago, Chicago, IL 60637 USA;  
t-oka@uchicago.edu*

<sup>2</sup>*Gemini Observatory, Hilo, HI 96720 USA*

(Accepted by ApJ, 2020 Aug 21)

### ABSTRACT

Velocity profiles of a line of H<sub>3</sub><sup>+</sup> at 3.7 μm produced in warm diffuse gas have been observed toward 18 stars in the Central Molecular Zone (CMZ) of the Galaxy. Their longitude-velocity diagram indicates that the gas is radially expanding within the CMZ at speeds up to a maximum of ~150 km s<sup>-1</sup>. The current momentum and energy in the gas are ~ 5 × 10<sup>8</sup> M<sub>⊙</sub> km s<sup>-1</sup> and ~ 5 × 10<sup>53</sup> erg. The motion is similar to that of the Expanding Molecular Ring (EMR) discovered in 1972 by Kaifu et al. and by Scoville. We propose that the expanding gas seen in H<sub>3</sub><sup>+</sup> is part of the same phenomenon, in spite of differences in estimates of density, morphology, and degree of rotation. The outward motion suggests that one or more ejection events occurred near the center of the CMZ (0.5–1) × 10<sup>6</sup> years ago, which may be related to creation of the recently observed microwave bubble. These observations revive the circular face-on view of the CMZ proposed in 1972, which fell out of favor after 1991 when Binney et al. proposed that a face-on view of the CMZ would show it to have an elliptical shape, with high eccentricity. While that model may apply on kiloparsec scales, we argue that it is incorrect to apply it to the much smaller CMZ. We discuss the fate of the expanding gas, which appears to be eventual infall into the center, leading to episodes of star formation and violent events associated with accretion onto Sgr A\*.

*Keywords:* Astrochemistry — cosmic rays — Galaxy:center — infrared:stars — ISM:Lines and Bands — ISM:molecules— ISM:cloud — ISM:structure

### 1. INTRODUCTION

On the night of July 10-11, 1997 at the United Kingdom Infrared Telescope (UKIRT) spectra toward two bright stars in the Galaxy’s Central Molecular Zone (CMZ), the central 300 pc of the Galaxy, revealed unexpectedly high column densities of H<sub>3</sub><sup>+</sup> (Geballe et al. 1999). One of the stars, GCIRS 3, is in the Central Cluster of massive luminous stars centered on the supermassive black hole, Sgr A\*. The other, known as GCS 3-2, is located in the Quintuplet Cluster, 30 pc to the east of Sgr A\*, and is also deeply embedded in the CMZ. The column density of H<sub>3</sub><sup>+</sup> toward each of these stars is an order of magnitude higher than the column densities of H<sub>3</sub><sup>+</sup> that had been measured toward young stellar objects in dense clouds and toward a star in a diffuse cloud, all of which are located in the Galactic disk (Geballe & Oka 1996; McCall et al. 1998, 1999). This striking difference exists despite the extinctions to the two stars in the GC stars being comparable to and in some cases lower than the extinctions to the young stellar objects, and only three times higher than the extinction to the diffuse cloud source. Consequently the 3.5–4.0 μm infrared spectrum of H<sub>3</sub><sup>+</sup> (Oka 1980), or trihydrium, a molecular ion having several unique and valuable properties

for studies of the interstellar medium, has emerged as a novel probe to investigate the gaseous environment in the CMZ.

Further observations and analysis in the first decade of this century established that the CMZ in the region from Sgr A\* to 30 pc east contains long columns of warm (~200 K) low density (< 100 cm<sup>-3</sup>), and mostly blueshifted gas (Goto et al. 2002; Oka et al. 2005; Goto et al. 2008). In 2008 a program was launched to search for bright stars throughout the CMZ with smooth continua in order to extend studies of H<sub>3</sub><sup>+</sup> from the central 30 pc to cover the full 300 pc extent of the CMZ (Geballe & Oka 2010). The project has been completed (Geballe et al. 2019a) and has provided ~30 suitable stars extending from 140 pc west of Sgr A\* to 116 pc east (herein we use a GC distance of 8 kpc). A comprehensive analysis of spectra of H<sub>3</sub><sup>+</sup> and CO observed during the last 20 years, including many of these newly found objects, has recently been published (Oka et al. 2019, hereafter Paper I). This has led to two conclusions: (1) the predominance in terms of volume of warm and diffuse gas in the CMZ; and (2) the high cosmic ray ionization rate (ζ ~ 10<sup>-14</sup> s<sup>-1</sup>) in the CMZ, 1000 times higher in dense clouds (Geballe & Oka 1996; McCall et al. 1999) and 100 times higher than in diffuse clouds in the Galactic disk (McCall et al. 2003; Indriolo et al. 2007; Indriolo & McCall 2012). As corollaries, Paper I showed that

the CMZ is not as opaque as reported in some papers (e.g. Morris & Serabyn 1996) and concluded that ultra-hot X-ray-emitting gas does not exist continuously and extensively in the CMZ as reported in some papers (Koyama et al. 1989; Lazio & Cordes 1998, see their Fig. 9).

In this paper, Paper II, we report the results of our investigations of the dynamics and morphology of this warm and low density gaseous environment, obtained from the velocity profiles of  $\text{H}_3^+$  lines. We take advantage of properties of the absorption profiles produced in dense clouds within the CMZ and the foreground spiral arms: that they tend to be sharp and occur at radial velocities known from previous radio and millimeter wave spectroscopy. In contrast, the profiles of  $\text{H}_3^+$  lines arising within the CMZ, in addition to frequently being broad, occur predominantly in warm diffuse gas, an environment that is usually straightforward to differentiate from gas in dense clouds via spectroscopy of several  $\text{H}_3^+$  lines and lines of the first overtone band of CO. The velocity dispersions of the  $\text{H}_3^+$  lines arising in the warm diffuse gas along the line of sight are as high as  $150 \text{ km s}^{-1}$ , a unique feature of the CMZ. We make use of the longitude-velocity ( $l, v$ ) diagram (e.g. Binney & Merrifield 1998, Section 9.1) of this gas to draw simple and straightforward conclusions regarding its dynamics and morphology.

## 2. PREVIOUS OBSERVATIONS AND INTERPRETATIONS

### 2.1. Early Observations

The highly blueshifted line profiles that play a central role in this paper were first observed in the 21 cm HI emission spectrum by Rougoor & Oort (1960). Due to the very low spatial resolution, the observed maximum positive and negative velocities of  $135 \text{ km s}^{-1}$  were interpreted by them as the maximum tangential velocity of a circular motion (see Fig. 4 of Rougoor & Oort (1960), Fig. 1 of Rougoor (1964), and Fig. 9 of Oort (1977)). However, based on a separate survey of high velocity HI emission van der Kruit (1970) had proposed an expulsion of gas from the Galactic nucleus.

When molecular radio astronomy was initiated with observation of the 18 cm  $\Lambda$ -doublet OH absorptions (Weinreb et al. 1963), five papers were published in 1964 on OH absorption in the GC using Sgr A as the background radio continuum source (Bolton et al. 1964a; Dieter & Ewen 1964; Robinson et al. 1964; Goldstein et al. 1964; Bolton et al. 1964b) primarily because it is bright. Among them Fig. 2 of Robinson et al. (1964) most clearly demonstrated the existence of the  $-135 \text{ km s}^{-1}$  absorption toward Sgr A. Readers are referred to Whiteoak (1994) for more details of the spectra and interesting anecdotes of the Australian OH observations. Unlike the HI emission, which does not allow one to determine if the high velocity gas is situated in front of or behind Sgr A, the intense OH absorption demonstrated that a large amount of gas is moving outward from the GC at high velocity. Later Robinson & McGee (1970) and McGee (1970) reported their extensive survey of one of the  $\Lambda$ -doublet lines at 1667 MHz from Galactic longitude  $357^\circ 30'$  to  $3^\circ 20'$ , measuring charac-

teristic radial velocities, velocity dispersions, sizes, and maximum values of apparent opacities for 63 clouds.

### 2.2. The Expanding Molecular Ring (EMR)

Based on the ( $l, v$ ) diagram of the radio OH absorption in Fig. 4 of McGee (1970) obtained using the 64 m Parkes Radio Telescope (angular resolution  $12'2$ ), Kaifu, Kato, & Iguchi (1972) proposed the existence of an Expanding Molecular Ring (EMR), a circular ring of radius 220 pc (adjusted to the GC distance of 8 kpc used herein) with expansion and tangential velocities of  $130 \text{ km s}^{-1}$  and  $50 \text{ km s}^{-1}$ , respectively; observations of the rear part of the ring were supplemented by measurements of  $\text{NH}_3$  emission at two positions. Kaifu et al. also pointed out the existence of the ring in the ( $l, v$ ) diagram of radio  $\text{H}_2\text{CO}$  absorption in Fig. 3a of Scoville, Solomon, & Thaddeus (1972) albeit with less angular coverage.

In a paper received 16 days after Kaifu, Kato, & Iguchi (1972), Scoville (1972), using the 43 m Green Bank Telescope, also proposed the existence of the EMR, based on the ( $l, v$ ) diagram of an  $\text{H}_2\text{CO}$  absorption line, but with a somewhat smaller radius 170 pc (adjusted) and expanding and tangential velocities of  $145 \text{ km s}^{-1}$  and  $50 \text{ km s}^{-1}$ , respectively. These values are taken from Model I of Scoville's Table I; we ignore Model II (Scoville also mentions that "contraction cannot be ruled out"). According to both papers the EMR is situated in the Galactic plane. In estimating the total mass of the EMR both papers assumed gas densities on the order of  $10^3\text{--}10^4 \text{ cm}^{-3}$ ; it is now thought that the observed gas is more likely to be mostly lower density (see Section 5.3.1).

Two years later Kaifu, Iguchi, & Kato (1974) reported "an almost complete ring" from observations of HI 21 cm absorption in front of Sgr A and emission behind it. We show the inferred face-on views of the CMZ of Kaifu, Kato, & Iguchi (1972) and Scoville (1972) in Figure 1, because the circular shape of the CMZ and expansion at  $\sim 140 \text{ km s}^{-1}$  are similar to what we conclude in this paper on the morphology and motion of the warm and diffuse gas within the CMZ. Note that the geometry and expansion of the EMR were derived from absorption spectra. Unlike the motions of dense gas in the GC, which have been explained as responses to the gravitational potential (see the next section), there is no way to explain the EMR in that way. (See Liszt & Burton (1980), however, for an explanation of a larger scale expanding arm as the result of the gravitational potential.) The motion of the EMR must be due to a massive expulsion of gas in the relatively recent past (see Section 6.2).

For a recent 3-dimensional analysis of the EMR as an expanding molecular shell (Sofue 1995b) and an expanding molecular cylinder (Sofue 2017) based on radio CO emission, see the next subsection.

### 2.3. The Galactic Center Ring (GCR)

Many molecules have been used to produce ( $l, v$ ) diagrams subsequent to the proposed existence of the EMR. By far the one most extensively used is the CO molecule, whose radio emission arises virtually entirely in dense gas (Bania 1977;

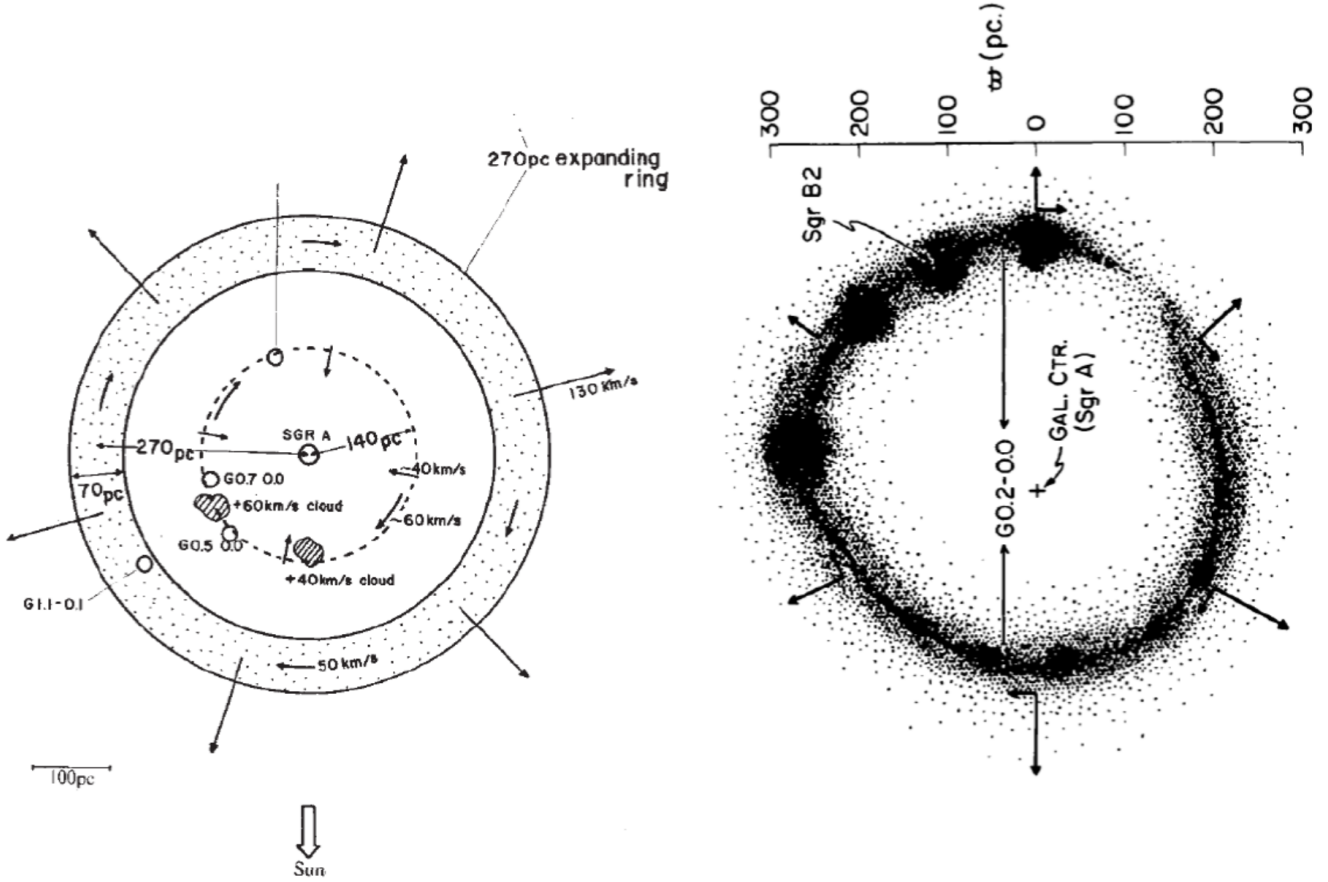


**Figure 1.** Face-on views of the Expanding Molecular Ring from Kaifu, Kato, & Iguchi (1972) (left) and Scoville (1972) (right). Note that the scales of the rings in pc in these figures are based on a GC distance of 10 kpc.

Liszt & Burton 1978; Heiligman 1987; Bally et al. 1987, 1988; Sofue 1995a,b; Dahmen et al. 1997; Oka et al. 1998a,b; Sawada et al. 2001; Martin et al. 2004; Oka et al. 2012). The slanted nearly linear section of the  $(l, v)$  diagram visible in Fig. 1e of Heiligman (1987), Fig. 4 (especially at  $b = 0.0$ ) of Bally et al. (1987), and Fig. 3 of Liszt (1992) indicate the presence of a rotating ring of dense gas. This was isolated in a detailed analysis of the data in Bally et al. (1987) by Sofue (1995a) and was called “the 120-pc molecular ring” (110 pc for the GC distance used in this paper). This ring of purely rotating dense clouds tilted by  $5^\circ$  and slightly bent has been widely accepted and named the Galactic center ring (GCR) by Rodríguez-Fernández et al. (2006). The “100 pc ring” observed in far-infrared emission by dust (Molinari et al. 2011) may be the same structure, although there are significant morphological differences. The active star forming regions Sgr B2 and Sgr C are often placed on the GCR.

Therefore, there appeared to be two rings, the outer EMR with a radius of  $\sim 200$  pc which suggested some explosive event near the Galactic nucleus within a million years (see Section 6), and the inner rotating circular GCR of dense gas with a radius of  $\sim 100$  pc which is the response to the central gravitational potential. Subsequently the GCR has been reinterpreted as composed of two spiral arms, Arm I and Arm

II (see Figs. 2 and 3 of Sofue (1995a) and Fig. 3 of Sofue (1995b), Sawada et al. (2004), Henshaw et al. (2016), Ridley et al. (2017), and others).

Sofue’s three-dimensional analysis of the CO emission observed by Bally et al. (1987, 1988) also significantly altered the concept of the EMR (Sofue 1995b). Instead of a planar structure he found a structure with vertical extent of  $\pm 50$  pc and called it the Expanding Molecular Shell (EMS). More recently, from a three-dimensional analysis of more extensive observations by Oka et al. (1998b), Sofue (2017) showed that the EMR is a bi-polar vertical cylinder with the total length as great as 170 pc and called it the Expanding Molecular Cylinder (EMC). He also identified the GCR with the CMZ and estimated that the mass of the CMZ is higher than that of EMC by a factor of  $\sim 8$ . His estimate of the mass of the EMR/EMC of  $0.8 \times 10^7 M_\odot$  is in good agreement with the mass of  $6 \times 10^6 M_\odot$  (Table 7 of Paper I). See also Henshaw et al. (2016).

#### 2.4. Barred potential and elliptical orbit with high eccentricity

The interpretation of the gas in the CMZ as having a largely circular distribution, as suggested by the EMR and GCR, was drastically modified by Binney et al. (1991), who developed a theory of gas motion in the Galactic barred potential (see

also Athanassoula 1992a,b). They demonstrated that for longitudes within  $10^\circ$  ( $\sim 1,500$  pc) of the center the motions of dense clouds observed in mm wavelength lines of CO and CS can be accounted for by two closed orbits,  $x_1$  and  $x_2$ , so named by Contopolous & Mertzanides (1977) in their non-linear theory of inner Lindblad resonances in galaxies (Lindblad (1927); see also Contopolous (1975)). The  $x_2$  orbit is circular and hence its  $(l, v)$  diagram is a straight line while the  $x_1$  orbit is an ellipse of high eccentricity, with sharp cusps at the two ends and its  $(l, v)$  diagram resembles a parallelogram (see Figs. 1 and 3 of Binney et al. 1991). The theoretical calculation appears to reproduce the large scale  $(l, v)$  diagram of the 21 cm HI emission observed by Burton & Liszt (1978) in which the longitudinal coverage is  $\sim 3$  kpc. There exist some similarities between the calculated  $x_1$  orbit and observed face-on views of external galaxies (e.g., Regan et al. 1999). The ellipse is seen clearly in the observed face-on views of external galaxies with bars within bars, e.g., Fig. 1a-d of Friedli & Martinet (1993) and Fig. 14 of Kormendy & Kennicutt (2004). The  $x_1$  orbit applied to gas on the scales of kiloparsecs seems to be well supported by observations. Many additional studies of the Lindblad resonance applied to large scale GC gas distribution and kinematics have been published (e.g. Sormani, Binney, & Magorrian 2015a,b,c; Suzuki et al. 2015).

However, application of the theory in Sections 3, 4, and 5 of Binney et al. (1991) to the more than 10 times smaller volume of the CMZ is questionable. Unlike on kiloparsec scales there is no observational evidence in the CMZ for the existence of a barred potential (Kruijssen, Dale, & Longmore 2015). Therefore there is no reason for the existence of an ellipse with high eccentricity which surrounds a bar. In the nuclear spirals model of Ridley et al. (2017), based on the two spiral arms reported by Sofue (1995a) and Sawada et al. (2004), the  $x_1$  orbit is introduced *a priori* as connecting to Arm I of Sofue (1995a), but the source of the barred potential causing the  $x_1$  orbit is not identified. We conclude that the resemblance of the  $(l, v)$  diagram of CO emission in the CMZ to an off-center parallelogram in Fig. 2 of Binney et al. (1991) (from Bally et al. (1988); see also Blitz et al. (1993)) must be incidental and that the face-on view of the CMZ as an ellipse with extremely high eccentricity, which appears for example in Fig. 2 of Rodríguez-Fernández et al. (2006), Fig. 21 of Bally et al. (2010), and Fig. 4 of Tsujimoto et al. (2018), is a chimera. Nevertheless the elliptical  $x_1$  orbit has become popular and the notions of an EMR and the face-on view of the CMZ being circular seem to have taken a back seat. Few papers have been published on the EMR after Sofue (1995b). The “EMR” in Fig. 12 of Sawada et al. (2004) is a misnomer since the gas motion is tangential to the ring. Our analysis of the observations presented in this paper revives the circular face-on view of the CMZ shown in Fig. 1.

### 2.5. $H_3^+$ as a probe for dynamical and morphological studies of the CMZ

The most extensive spectroscopic survey of gas in the CMZ has been that of the CO  $J = 1 \rightarrow 0$  emission line by

Oka et al. (1998b) (Tomoharu Oka of Keio University, not to be confused with the first author of the present paper). Emission from this line nearly completely covers the CMZ. In comparison, the high-resolution  $H_3^+$  absorption spectroscopy of CMZ gas reported here has the serious drawback that observations are limited to sightlines to bright stars with smooth infrared continua (Geballe et al. 2019a). As mentioned in the Introduction, such stars are rare. Moreover, while the 45-m radio dish used by Oka et al. (1998a) and Oka et al. (1998b) has a beam width of  $16''$  corresponding to  $\sim 0.62$  pc and observed the frequently highly saturated  $J = 1 \rightarrow 0$   $^{12}\text{C}^{16}\text{O}$  emission, the narrow sightline toward the infrared stars (diameters on the order of  $0''.00001$ ,  $\sim 0.1$  AU), can completely miss localized dense clouds. Because of the limited sightlines available, the infrared absorption spectroscopy of  $H_3^+$  and CO that we have employed is not useful for surveys of dense clouds in the CMZ.

Despite its limitations the  $H_3^+$  absorption spectrum is a powerful probe for surveying the warm and diffuse gas which dominates the CMZ (volume filling factor  $\sim 2/3$ ; Paper I). Although the number of observed sightlines is limited, each sightline probes a long  $H_3^+$  column, as long as the star used as a background source is deeply embedded in the CMZ. The  $(l, v)$  diagram derived from the  $H_3^+$  spectrum provides significant information on the dynamics and morphology of the gas in the CMZ. Absorption spectroscopy is limited to sampling gas in front of the stars, but it has the great advantage of discriminating between motions toward and away from the GC. We note that most of the  $H_3^+$  absorption lines observed toward stars in the GC are blueshifted and broad, with velocities ranging from  $\sim -150$  to  $\sim +10$   $\text{km s}^{-1}$ . This clearly demonstrates that the diffuse gas in the CMZ is moving away from the center rather than falling into the center as has been suggested for dense gas (e.g. Morris & Serabyn 1996). Such gas motions had been noted earlier from radio observations of absorption by  $\text{HCO}^+$  toward Sgr B2 (Linke, Stark, & Frerking 1981) and absorption by  $\text{H}_2\text{CO}$  and H I toward Sgr A (Güsten & Downes 1981). As shown in this paper, spectroscopy of  $H_3^+$  demonstrates that the expanding gas exists widely in the CMZ.

The peak optical depths of the strongest lines of  $H_3^+$  are at most 0.1. Thus unlike the intense radio CO emission spectrum, where analysis faces the complication of radiation trapping (Scoville & Solomon 1974; Goldreich & Kwan 1974), the observed equivalent widths are linearly related to  $H_3^+$  column densities to a good approximation. This makes the interpretation of the observed  $H_3^+$  spectra direct and simple when viewing dynamical and morphological data. The same is true for lines of the  $v = 2 \leftarrow 0$  overtone band of CO near  $2.34 \mu\text{m}$ , unlike the 130 times stronger CO fundamental band at  $4.5\text{--}5.0 \mu\text{m}$  and the pure rotational CO millimeter wave lines.

### 2.6. $H_3^+$ as a probe of density and temperature

Although not a key part of this paper and covered in previous papers (e.g., Paper I), it is worth summarizing here the unique properties of  $H_3^+$  that allow one to unambiguously

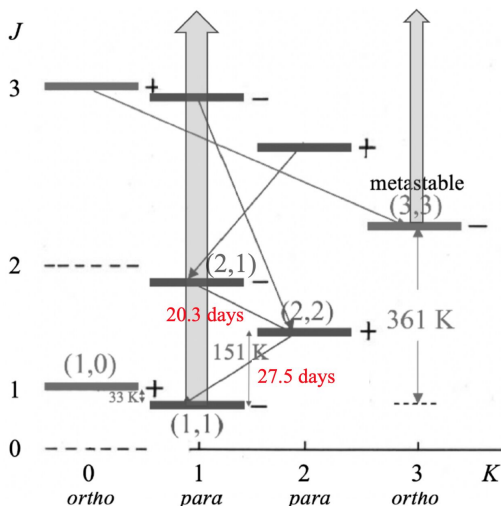


**Figure 2.** Rotational levels of  $\text{H}_3^+$  in the ground vibrational state. This paper is based mainly on velocity profiles of the  $R(1,1)^l$  ro-vibrational transition from the ground  $(1,1)$  level (wide arrow), with the  $R(3,3)^l$  line (narrow arrow) providing supplementary information. Lifetimes of the  $(2,1)$  and  $(2,2)$  levels are shown. For the notation  $R(1,1)^l$  etc. see Lindsay & McCall (2001), Oka (2013), or Miller et al. (2020).

detect and characterize the low density and warm temperature of the gas in the CMZ (Paper I). These properties are illustrated by the energy level diagram in Figure 2 and are described below.

At typical cloud temperatures in the Galactic disk (a few tens of degrees) only the two lowest energy levels of the ground vibrational state of  $\text{H}_3^+$  ( $J, K$ ) =  $(1,1)$  and  $(1,0)$  are populated. At higher temperatures the next three lower levels,  $(2,1)$ ,  $(2,2)$ , and  $(3,3)$  may come into play. Because  $\text{H}_3^+$  in the  $(3,3)$  level cannot radiatively decay, if temperatures are sufficiently high this level has a significant population and an ro-vibrational absorption line from it at  $3.53 \mu\text{m}$ , the  $R(3,3)^l$  line, is detectable. This situation exists in the CMZ and to date has been found nowhere else. On all sightlines observed toward stars in the CMZ, the ratio of this line to those from the lowest lying lines from  $J = 1$  yield temperatures in the CMZ of  $\sim 200$  K (Paper I).

The  $(2,1)$  and  $(2,2)$  para-levels lie below the  $(3,3)$  level and thus can be collisionally excited at temperatures at which the  $(3,3)$  level is populated, as well as at somewhat lower temperatures. However, both of those levels radiatively decay, with lifetimes of  $\sim 20$  and  $27$  days, respectively (Mizus et al. 2017; Neale, Miller, & Tennyson 1996), as illustrated in Figure 2, due to the spontaneous breakdown of symmetry (Oka et al. 1971; Pan & Oka 1986). The critical densities for these levels are each  $\sim 200 \text{ cm}^{-3}$  (Oka & Epp 2004). At densities lower than that significant populations in these levels are not maintained and lines originating from them will be weak or absent. The presence of the absorption line from  $(3,3)$  and the complete absence of lines from  $(2,2)$  on nearly all sightlines in the CMZ (Paper I) clearly demonstrate that the CMZ gas

in which the  $\text{H}_3^+$  resides is of low mean density, most likely  $\sim 50 \text{ cm}^{-3}$  (Paper I).

### 3. OBSERVATIONS

Spectra in this series of papers have been obtained using five infrared spectrographs at five telescopes, three in Hawaii and two in Chile. Most of the data were acquired by the Phoenix Spectrometer (resolving power  $R \sim 60,000$ ) on the 8.1-m Gemini South Telescope. Some spectra were obtained by Cold Grating Spectrometer 4 (CGS4,  $R \sim 40,000$ ) on the 3.8-m United Kingdom Infrared Telescope (UKIRT), the Cryogenic Infrared Echelle Spectrograph (CRIRES,  $R \sim 50,000$  and  $100,000$ ) on the 8.2-m Very Large Telescope (VLT), and the Gemini Near-Infrared Spectrograph (GNIRS,  $R \sim 20,000$ ) on the 8.1-m Frederick C. Gillett Gemini North telescope. Details of the spectrometers and data reduction are given in Section 2.3. of Paper I.

#### 3.1. Bright dust-embedded stars used for the $\text{H}_3^+$ spectroscopy

The observations were limited to bright ( $L \leq 7.7$  mag) dust-embedded stars with smooth infrared continua in the  $3.5\text{--}4.0 \mu\text{m}$  region and bright emission line stars whose lines did not coincide with important lines of  $\text{H}_3^+$ . Both types of stars allow sensitive high-resolution spectroscopy of the key lines of  $\text{H}_3^+$ . Altogether spectra of the  $R(1,1)^l$  line toward 29 stars have been obtained; they are listed in Table 2 of Paper I. In this paper, to characterize the gas in front of the central region of the CMZ from Sgr A\* to 30 pc to the east, we present spectra of two stars in the Central Cluster (Becklin & Neugebauer 1975; Becklin et al. 1978; Viehmann et al. 2005), two stars between the Central Cluster and the Quintuplet Cluster, and five stars in the Quintuplet Cluster (Kobayashi et al. 1983; Nagata et al. 1990; Okuda et al. 1990). Three of these are NHS stars, found by Nagata et al. (1993) and one is an FMM star (Figer, McLean, & Morris 1999). All nine are high mass stars and all but two were known prior to the Geballe et al. (2019a) survey. All exhibit strong absorption lines of  $\text{H}_3^+$  indicating simultaneously their similar depths in the CMZ, the ubiquity of  $\text{H}_3^+$  in the gas in front of the central 30 pc, and the abundance of the warm and diffuse gas in which that  $\text{H}_3^+$  resides.

To study the gas in the rest of the CMZ we have observed 13 of the suitable stars scattered across the CMZ, from 140 pc to the west of Sgr A\* to 116 pc to the east, newly found by the Geballe et al. (2019a) survey. The spectra of nine of them are presented here. Several additional stars were found to be foreground stars, but based on the strengths of their  $\text{H}_3^+$  absorption lines, these nine stars are located deeply enough in the CMZ to provide valuable data. All of the newly found stars were known only by their coordinates in the Two-Micron All Sky Survey (2MASS) catalogue. For convenience of memory and discussion in Paper I we unofficially designated the newly found stars using the Greek alphabet  $\alpha$  to  $\lambda$  from the west to east. As the survey found more suitable stars we designated them by  $\alpha-$ ,  $\alpha+$ ,  $\alpha+-$ , etc. We use these designations here.

The newly found stars tend to be clustered. For example, close to the western edge of the CMZ and nearly on the Galactic plane three suitable stars were found ( $\alpha$ ,  $\alpha+$ , and  $\beta$ ). No stars were found that close to the eastern edge; the closest are stars  $\lambda-$  and  $\lambda+$ . The stars do not provide an ideally sampled  $(l, v)$  diagram, but still provide enough information for a detailed study to be feasible and for key conclusions to be drawn.

The 18 stars whose spectra are reported here are listed in Table 1. The table includes the  $L$  magnitudes of the stars, their Galactic longitudes, their distances from Sgr A\* on the plane of the sky in the longitudinal (EW) direction, their latitudinal (NS) distances from the Galactic plane, and the ranges of LSR absorption velocities of warm diffuse gas observed in  $H_3^+$ .

### 3.2. Observed velocity profiles of $H_3^+$ : the CMZ's contribution

In this subsection we illustrate the general approach to understanding the absorption spectra of  $H_3^+$  lines toward stars in the CMZ by presenting and analyzing the velocity profiles of  $H_3^+$  and CO absorption lines toward the bright infrared source GCS 3-2, located in the Quintuplet Cluster. Profiles of some of the lines observed toward it are shown in Figure 3.

#### 3.2.1. The $R(1,1)^l$ spectrum: subtraction of spectra in spiral arms

For investigating velocity profiles of spectral lines of  $H_3^+$ , the  $R(1,1)^l$  transition at  $2691.443 \text{ cm}^{-1}$  ( $3.71548 \mu\text{m}$ , thick arrow in Figure 2) arising from the ground  $(1,1)$  level and having the transition dipole moment  $0.119 \text{ D}$ , is the optimal choice; it is the strongest line, it is relatively free from atmospheric interference, and its intensity is nearly independent of temperature.

A complication in interpreting the absorption velocity profile of this line is that absorption by  $H_3^+$  can be produced not only in the CMZ, but also in the three foreground spiral arms (see the top trace of Figure 3). Fortunately, in dense clouds absorption lines are also produced by CO, whose overtone band can be used to clearly identify the contribution of foreground absorption to the  $H_3^+$  line profiles. In addition the absorption lines in spiral arm clouds are almost always narrow and occur at characteristic radial velocities. These aspects are illustrated in Figure 3, where one can see three sharp optically thin absorption components in a  $2.34\text{-}\mu\text{m}$  CO overtone line (bottom trace), and similar features contributing to the  $H_3^+ R(1,1)^l$  line profile (top trace). The three sharp absorptions in both spectra at  $\sim -50 \text{ km s}^{-1}$ ,  $\sim -30 \text{ km s}^{-1}$ , and  $\sim 0 \text{ km s}^{-1}$  correspond to the velocities of gas in the 3 kpc arm (Rougoor & Oort 1960), the 4.5 kpc arm (Menon & Ciotti 1970) and the local arm, respectively. Each of these absorptions has a small velocity gradient with longitude, which is used for studies of kinematics and dynamics of the gas (e.g. Sofue 2006). It is relatively straightforward to subtract them from the  $H_3^+ R(1,1)^l$  profile to elucidate the spectrum of  $H_3^+$  in the CMZ. After the subtraction, the  $R(1,1)^l$  absorption is an uneven trough with the approximate shape of the shaded polygon in the third trace of Figure 3.

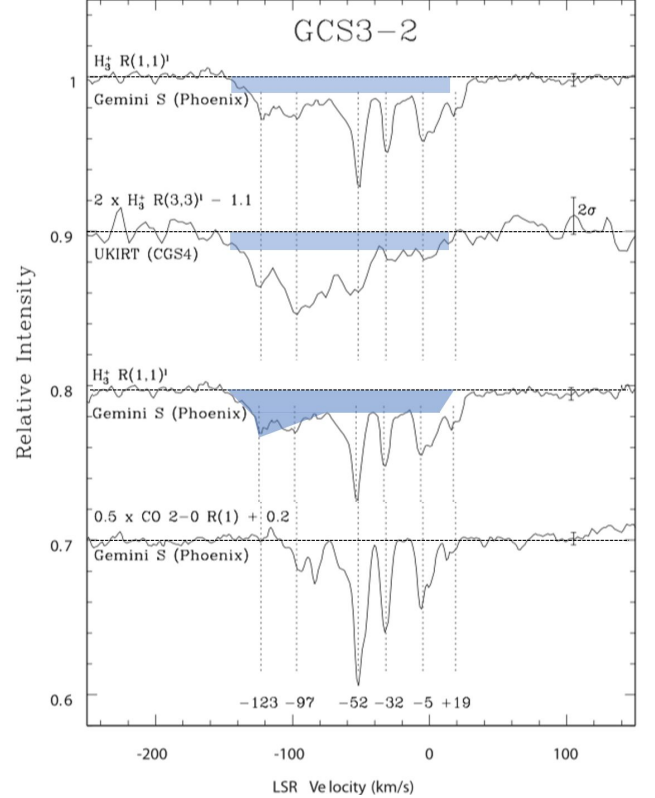


**Figure 3.** Velocity profiles of  $H_3^+$  and CO lines toward the star GCS 3-2 adapted from Oka et al. (2005)). Horizontal dashed lines indicate the continuum. Top trace:  $R(1,1)^l$  profile (see Section 3.2.1.). Second trace:  $R(3,3)^l$  profile (see Section 3.2.2.). Third trace: same as top trace, but with absorptions of  $H_3^+$  in the dense clouds in the foreground spiral arms subtracted, to produce the shaded area, which is that part of the  $R(1,1)^l$  profile originating in the CMZ. Bottom trace: CO  $v = 2 \leftarrow 0 R(1)$  profile, with narrow and deep absorptions produced mainly at approximately  $-52$ ,  $-32$ , and  $0 \text{ km s}^{-1}$  by dense clouds in the three foreground spiral arms. The shaded rectangles in the upper two spectra depict the velocity extent of the warm diffuse CMZ gas.

As will be illustrated in Section 4, on sightlines more distant from the central region, the velocity dispersion of the CMZ gas decreases with distance. Near the western edge of the CMZ, where suitable stars are available to probe the gas, the dispersion nearly vanishes, as the motion of the gas is largely perpendicular to the line of sight. At these locations it is more challenging to separate the absorption in the  $R(1,1)^l$  line due to CMZ gas from that of local arm (except for the case of the sightline toward Star  $\alpha$ ; see Section 4.7). In these cases observations of the  $R(3,3)^l$  line, which is absent in the low temperature gas of the spiral arms, are critical for identifying the presence of low velocity warm diffuse gas in the CMZ. More details on the spectral features arising in

**Table 1.** Observed  $\text{H}_3^+$   $R(1,1)^l$  Spectra

Stars	$L$ (mag) <sup>a</sup>	$G_{\text{lon}}$ (°)	EW (pc)	NS (pc)	Velocity range (km s <sup>-1</sup> ) <sup>b</sup>	Note
$\alpha$	3.79	-1.0463	-138.7	-2.65	(-15, 15)	narrow line
$\alpha+$	7.02	-1.0417	-138.0	-6.12	(-25, 25)	narrow line
$\beta$	4.53	-1.0082	-133.4	-4.20	(-15, 15)	narrow line
$\gamma$	6.41	-0.5442	-68.4	-6.48	(-165, -110)	narrow line
$\delta$	6.51	-0.2834	-31.9	1.57	(-163, -116) (-93, 26)	two troughs
GCIRS 3	4.84	-0.0576	-0.15	0.07	(-150, ~0)	trough
GCIRS 1W	4.92	-0.0549	0.06	0.15	(-145, ~0)	trough
$\epsilon+$	7.56	0.0300	12.0	-5.88	(-158, ~0)	trough
NHS 21	4.60	0.0992	21.7	-1.27	(-145, -103) (-90, ~0)	two troughs
NHS 42	6.61	0.1479	28.5	0.50	(-147, 17)	trough
NHS 25	5.63	0.1591	30.1	-2.69	(-156, 16)	trough
$\eta$	5.52	0.1631	30.6	-3.92	(-160, ~0)	trough
GCS 3-2	3.16	0.1635	30.7	-2.00	(-145, 15)	trough
FMM 362	6.41	0.1787	32.8	-2.67	(-145, -20)	trough
$\theta$	6.38	0.2647	44.9	-3.86	(-160, -30) (-15, 15)	two troughs
$\iota$	6.58	0.5477	84.5	-1.83	(-115, -40)	trough
$\lambda-$	6.72	0.7685	115.5	-28.54	(-52, 20)	trough
$\lambda - +$	7.06	0.7746	116.2	21.98	(-80, ~0)	trough

<sup>a</sup>Magnitudes from GLIMPSE IRAC 1 filter, Ramirez et al. 2008), except from Viehmann et al. (2005) for GCIRS 1W and GCIRS 3.

<sup>b</sup>Values within parentheses are in LSR and are minima and maxima of continuous ranges of absorption.

the foreground spiral arms can be found in Section 5.3.1 of Paper I.

### 3.2.2. The $R(3,3)^l$ spectrum: the fingerprint of $\text{H}_3^+$ in the CMZ

The  $R(3,3)^l$  line at  $2829.935 \text{ cm}^{-1}$  ( $3.53365 \mu\text{m}$ , narrow arrow in Figure 2), with transition dipole moment  $0.138 \text{ D}$ , arises from the metastable  $(3,3)$  level of ortho- $\text{H}_3^+$ . It is generally weaker than the  $R(1,1)^l$  line but its profile is free from contamination by foreground absorption because of the low temperature of gas in the spiral arms. Thus, it is the fingerprint by which  $\text{H}_3^+$  in the warm gas of the CMZ can be unambiguously identified.

Observing this line from ground-based telescopes can be challenging, however. The frequency of the  $R(3,3)^l$  line closely coincides with the strong  $2\nu_2 \nu_{05} \leftarrow 6_{34}$  transition of  $\text{H}_2\text{O}$  at  $2830.008 \text{ cm}^{-1}$ . The difference of  $0.073 \text{ cm}^{-1}$  corresponds to a Doppler shift of only  $8 \text{ km s}^{-1}$ . Since the distribution of atmospheric  $\text{H}_2\text{O}$  varies temporarily depending on the weather, and because the telluric absorption is strong and broad, correction for this line is more difficult than correcting for telluric absorption lines of other molecular species, especially at low radial velocities. This usually makes observations of the  $R(3,3)^l$  line from telescopes at the 4200-m summit of Maunakea Hawai'i (Subaru, Gemini North, UKIRT) more dependable than those from Cerro

Pachon (2715 m Gemini South) and Cerro Paranal (2635 m VLT) Chile.

The intensity of the  $R(3,3)^l$  line relative to that of the  $R(1,1)^l$  line is sensitive to the temperature of the gas. In the top trace of Figure 3 note that while the strength of the  $R(1,1)^l$  absorption trough toward GCS 3-2 (as well as those of several other centrally located stars) is roughly constant across most of its observed velocity range, the depth of the  $R(3,3)^l$  line (second trace in Figure 3) first increases toward more negative radial velocities until  $\sim -100 \text{ km s}^{-1}$ . This indicates increasing temperature of the gas with more negative velocities over the above range.

## 4. THE SPECTRA

In this section we present and describe the  $\text{H}_3^+$   $R(1,1)^l$  line profiles toward the 17 of the 18 selected stars (for GCS 3-2 see the preceding section). We begin with the two stars in the Central Cluster, move east to two stars in the region between the Central Cluster and the Quintuplet Cluster, and then further east to four stars in the Quintuplet Cluster itself. We then examine the  $R(1,1)^l$  velocity profiles of two stars approximately midway between the center and the eastern edge of the CMZ, and finally those of the two stars closest to the eastern edge, although still some 25 pc distant from the edge. To the west of the Central Cluster we show the

$R(1,1)^l$  profiles of two stars located between the center and the western edge of the CMZ, and lastly, the profiles of three stars located very close to the western edge.

In determining the presence and extent of the warm diffuse gas, in almost all cases we rely on the widths of the absorption troughs of the  $R(1,1)^l$  lines presented here and the published profiles of the  $R(3,3)^l$  line and/or CO overtone lines for guidance. We do not present the profiles of the  $R(3,3)^l$  line and CO lines here; the reader is referred to spectra of those lines in Goto et al. (2008), Geballe & Oka (2010), Goto et al. (2011), Goto et al. (2014), and Paper I.

#### 4.1. Central Cluster : GCIRS 3 and GCIRS 1W

Surrounding the black hole Sgr A\* and within a radius on the sky of 0.4 pc are many bright stars of the Central Cluster (see Fig. 2 of Viehmann et al. 2005), spectra of two of which are shown in Figure 4, GCIRS 3 (upper trace) and GCIRS 1W (lower trace). A significant difference between the sightlines toward these stars and that toward GCS 3-2 is that while the latter probes only diffuse clouds, the former sightlines cross dense gas in the circumnuclear disk (CND; Genzel & Townes 1987), which produces the absorption features in the two lines shown as well as in the  $R(2,2)^l$  line, at  $\sim 50 \text{ km s}^{-1}$  in GCIRS 3 and  $\sim 40 \text{ km s}^{-1}$  in GCIRS 1W (Goto et al. 2014). Discussions of these features is outside the scope of this paper.

Like the spectra of  $\text{H}_3^+$  lines toward GCS 3-2, spectra of GCIRS 3 and GCIRS 1W exhibit broad absorption troughs due to warm diffuse gas extending from  $-150 \text{ km s}^{-1}$  to near  $0 \text{ km s}^{-1}$ . At positive velocities the troughs merge with the absorption by the dense CND gas mentioned above. Therefore the velocities at these edges of the troughs are uncertain, and could be slightly positive. Also, unlike the spectra toward GCS 3-2 where the depth of the absorption trough varies fairly smoothly with velocity, the profiles toward GCIRS 3 and GCIRS 1W show significant variations of depth, indicating variations in the density of the warm diffuse gas with velocity, and presumably with radial location within the CMZ on these sightlines. Interestingly both the  $R(1,1)^l$  and  $R(3,3)^l$  lines have absorption features near the radial velocities of the three foreground spiral arms. On the other hand, spectra of CO overtone lines toward these sources also have prominent absorptions at all three velocities ( $-50$ ,  $-30$ , and  $0 \text{ km s}^{-1}$ ), while spectra of the  $R(2,2)^l$  line show no absorption except at the positive velocity of the CND (Goto et al. 2014). We therefore conclude that much of the deep absorptions in the  $R(1,1)^l$  line profile at these velocities is produced by dense gas in the spiral arms. However, because the metastable (3,3) level is not populated in the cold gas of the spiral arms, we also conclude that these three absorption features in the  $R(3,3)^l$  line are formed in the warm and diffuse gas in the CMZ, and only coincidentally approximately match the velocities of the foreground spiral arms.

#### 4.2. Stars between the Central Cluster and the Quintuplet Cluster : $\epsilon+$ and NHS 21

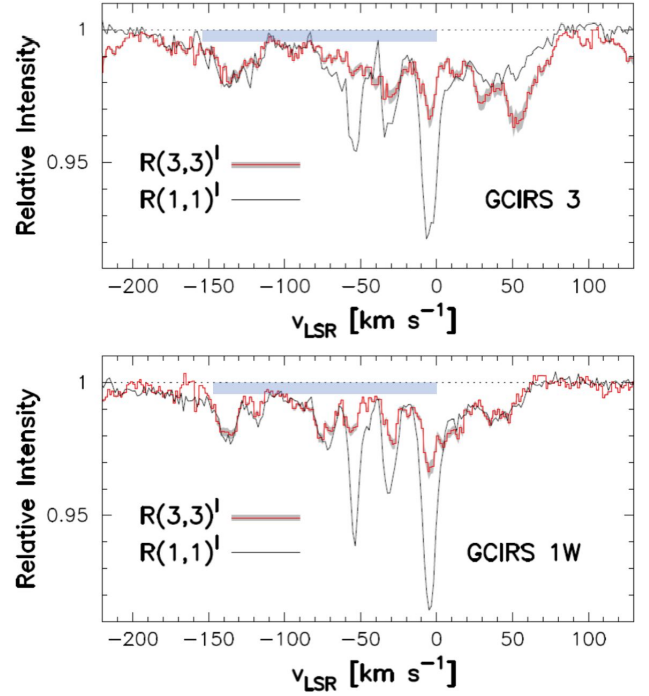


**Figure 4.** Velocity profiles of the  $R(1,1)^l$  and  $R(3,3)^l$  lines toward the Central Cluster stars GCIRS 3 (top) and GCIRS 1W (bottom), from Goto et al. (2014). The  $R(3,3)^l$  absorption has been scaled by a factor of 1.3 for ease of comparison. All spectra were recorded by the CRILES spectrometer at the VLT. Shaded rectangles indicate the extents of the warm diffuse CMZ gas (see Section 4.1).

Figure 5 contains the velocity profiles of the  $R(1,1)^l$  spectra toward two stars located between the Central Cluster and the Quintuplet Cluster,  $\epsilon+$  and NHS 21. Absorption from the former contains a broad shallow feature similar to that toward GCS 3-2, as well as the three sharp spiral arm features; the latter are also present in the spectrum of NHS 21. The broad absorption in the spectrum of NHS 21, however, has a gap from  $103 \text{ km s}^{-1}$  to  $-90 \text{ km s}^{-1}$ , with little or no absorption. It is tempting to conclude from this that NHS 21 is more shallowly embedded in the CMZ, but the similar depths of the troughs suggest otherwise. We suspect that NHS 21 lies deep within the CMZ, but that warm diffuse gas in the above narrow velocity range is simply absent on sightlines through that region of the CMZ.

#### 4.3. Quintuplet Cluster : GCS 3-2, NHS 42, NHS 25, $\eta$ , FMM 362

Spectra of  $\text{H}_3^+$  lines toward four of the five bright and closely spaced infrared Quintuplet stars, for which the Cluster is named: GCS 3-1, GCS 3-2, GCS 3-4, and GCS 4, were published in Paper I. The four are within 0.7 pc of one an-

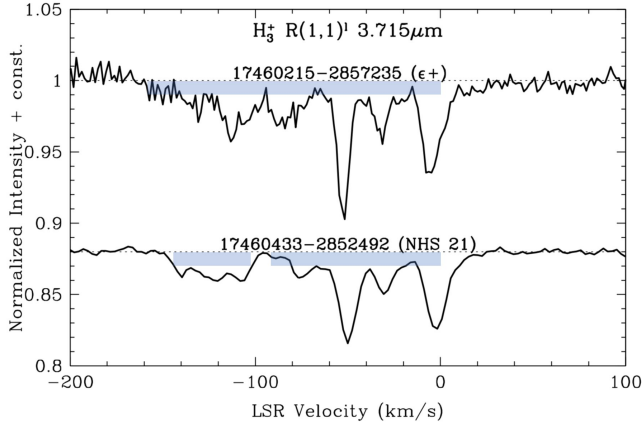


**Figure 5.** The velocity profiles of the  $R(1,1)^l$  line of  $\text{H}_3^+$  observed toward the Stars  $\epsilon+$  and NHS 21. Both spectra were obtained by the Phoenix Spectrometer at the Gemini South Observatory. Shaded rectangles indicate the extents of the warm diffuse CMZ gas (see Section 4.2).

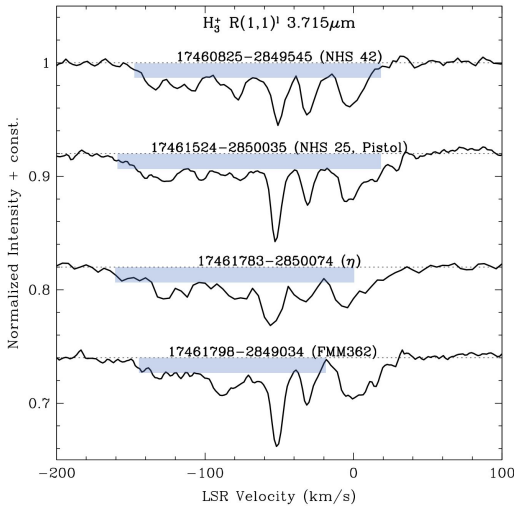


**Figure 6.** Velocity profiles of the  $R(1,1)^l$  lines observed toward four stars in the Quintuplet Cluster. All of the spectra were recorded by the Phoenix Spectrometer on the Gemini South telescope. Shaded rectangles indicate the extents of the warm diffuse CMZ gas (see Section 4.3).

other on the plane of the sky. Their velocity profiles are nearly identical (Paper I, Figure 3); Figure 3 of this paper, showing spectra of GCS 3-2, is a representative example. As discussed in Section 3.2, and illustrated in Figure 3, the CMZ produces a broad and almost entirely blueshifted absorption toward GCS 3-2 and the other members of the Quintuplet.

Figure 6 contains the velocity profiles of the  $\text{H}_3^+$   $R(1,1)^l$  line toward four other stars within the Quintuplet Cluster. Two of the stars, NHS 42 and FMM 362, are situated near opposite edges of the Cluster, which has a diameter of  $\sim 2$  pc

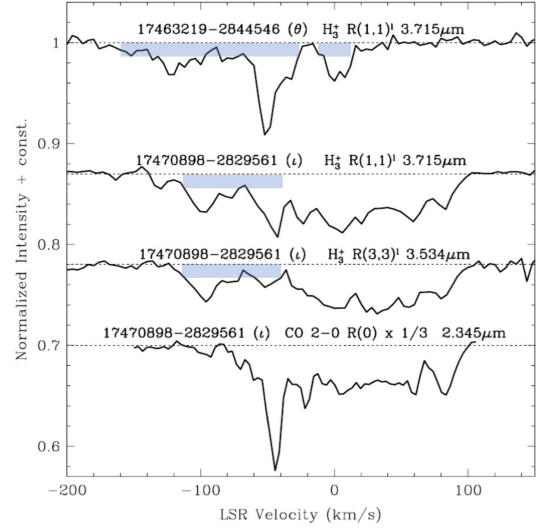


**Figure 7.** The velocity profiles of the  $R(1,1)^l$  line observed toward the Star  $\theta$  (top trace), and of the  $R(1,1)^l$  (second trace),  $R(3,3)^l$  (third trace), and CO  $v = 2 \leftarrow 0$   $R(0)$  (bottom trace) lines observed toward Star  $\iota$  near Sgr B. All spectra were recorded by the Phoenix Spectrometer at the Gemini South Observatory. Shaded rectangles indicate the extents of the warm diffuse CMZ gas (see Section 4.4).

(Figer, McLean, & Morris 1999). Once the foreground sharp spiral arm absorptions are removed, each of the four reveals a broad absorption trough of extent and shape generally similar to that of GCS 3-2. Many of the bright Quintuplet stars are known to possess energetic winds. However, the overall similarity of the CMZ profiles both toward them and toward the stars presented in Section 4.2, which are as much as 20 pc distant in the plane of the sky, is a convincing demonstration that the absorptions are not due to localized gas motions associated with any of the stars but are part of a much larger scale phenomenon.

#### 4.4. Stars roughly halfway to the eastern edge of the CMZ : $\theta$ and $\iota$

Figure 7 contains spectra toward two stars located 45 pc and 85 pc to the east of Sgr A\*. They lie between the Quintuplet Cluster and the suitable stars found in the survey that are closest to the eastern edge of the CMZ. Very roughly speaking these two stars are halfway between Sgr A\* and the eastern edge of the CMZ.

Interpretation of the  $R(1,1)^l$  spectrum toward Star  $\theta$  (top trace), which is the nearer of the two to the center, is somewhat of a challenge. Blueshifted absorption in this line extends to  $\sim -160$   $\text{km s}^{-1}$ . Its assignment to warm diffuse gas is consistent with our (unpublished) spectrum of the  $R(3,3)^l$  line, which shows absorption to approximately that velocity. At velocities more positive than  $-60$   $\text{km s}^{-1}$  absorption is contributed by  $\text{H}_3^+$  in the spiral arms near  $-51$   $\text{km s}^{-1}$  (3 kpc arm),  $-32$   $\text{km s}^{-1}$  (4.5 kpc arm) and  $-1$   $\text{km s}^{-1}$  (local arm), as attested to by the sharp absorption features in the CO overtone lines (see Fig. 6 of Paper I). However, the deep shoulder between the  $-51$   $\text{km s}^{-1}$  and  $-32$   $\text{km s}^{-1}$  features, which is

not observed toward other stars, suggests that the trough of absorption by warm diffuse gas extends to  $\sim -30 \text{ km s}^{-1}$ . The  $R(3,3)^l$  line profile also contains absorption in the  $-60$  to  $-30 \text{ km s}^{-1}$  interval. In addition, both the  $R(1,1)^l$  and  $R(3,3)^l$  lines show absorption from  $-15$  to  $+15 \text{ km s}^{-1}$ . The lack of absorption near  $-20 \text{ km s}^{-1}$  implies that the trough has a narrow gap centered near that velocity.

The sightline toward Star  $\iota$  (2MASS 17470898–2829561), located midway between Sgr B1 and Sgr B2, is unique in showing very broad, deep, and structured absorption profiles in lines of both  $\text{H}_3^+$  and the CO overtone band, extending from  $\sim -100 \text{ km s}^{-1}$  to  $\sim +100 \text{ km s}^{-1}$  (lower three traces of Figure 7; see also Geballe & Oka 2010). The strength of the CO absorption indicates that the CO is located in a number of dense clouds on this sightline. Because at positive velocities the pure rotational CO  $J = 1 - 0$  emission profile in Sgr B at this location (Oka et al. 1998a) roughly resembles these infrared profiles, Star  $\iota$  must be located within the Sgr B cloud complex. The sharp absorption at  $-43 \text{ km s}^{-1}$  in the CO  $R(0)$  line, other low  $J$  CO lines (Fig. 6 of Paper I), and in the  $\text{H}_3^+$   $R(1,1)$  line together with its absence in the  $\text{H}_3^+$   $R(3,3)$  line demonstrate that this feature is produced by dense gas in the 3 kpc arm. Nearly all of the rest of the absorption in this nearly  $200 \text{ km s}^{-1}$  wide interval arises within the CMZ.

At the highest negative velocities, between  $-70$  and  $-115 \text{ km s}^{-1}$ , absorption in the  $R(1,1)^l$  and  $R(3,3)^l$  lines is strong, but is virtually absent in CO (Figure 7) and in the  $R(2,2)^l$  line (Paper I, Fig. 8). Thus the absorbing  $\text{H}_3^+$  in this velocity interval is located in warm and diffuse gas in the CMZ. Absorption in the  $R(2,2)^l$  line is also weak or absent from  $-70$  to  $-40 \text{ km s}^{-1}$  (Paper I). Therefore, the  $R(3,3)^l$  absorption from  $-70 \text{ km s}^{-1}$  to  $-40 \text{ km s}^{-1}$  is also produced largely in diffuse gas. Thus, as found elsewhere in the CMZ, warm diffuse gas is present on this sightline over a wide range of negative velocities, in this case definitely from  $-115 \text{ km s}^{-1}$  to  $-40 \text{ km s}^{-1}$ . Warm diffuse gas may also be present at less negative than  $-40 \text{ km s}^{-1}$  as it is elsewhere; however, its unique signatures are hidden by the signatures of warm dense gas in this velocity range. Additional spectra and discussion of this interesting sightline will be presented in a separate paper (T. R. Geballe et al. in preparation).

#### 4.5. Stars Nearest to the Eastern Edge : $\lambda-$ and $\lambda-+$

The two stars whose  $R(1,1)^l$  spectra are shown in Figure 8,  $\lambda-$  and  $\lambda-+$ , are each  $\sim 25 \text{ pc}$  from the eastern edge of the CMZ. They are also much further displaced (in latitude) from the Galactic plane than any of the other stars in the sample. Nevertheless, their spectra provide evidence that the sightline to each of them passes through CMZ gas.

The  $R(1,1)^l$  line profile toward Star  $\lambda-$  (upper trace) shows absorption between  $\sim -90 \text{ km s}^{-1}$  and  $\sim +20 \text{ km s}^{-1}$ . The detection of absorption between  $\sim -90 \text{ km s}^{-1}$  and  $\sim -60 \text{ km s}^{-1}$  is clearly marginal; however the profile of the  $R(3,3)^l$  line in Paper I (Fig. 7) also shows continuous absorption in this velocity range (and extending continuously into positive velocities), and we therefore conclude that warm diffuse gas is present to velocities as far negative

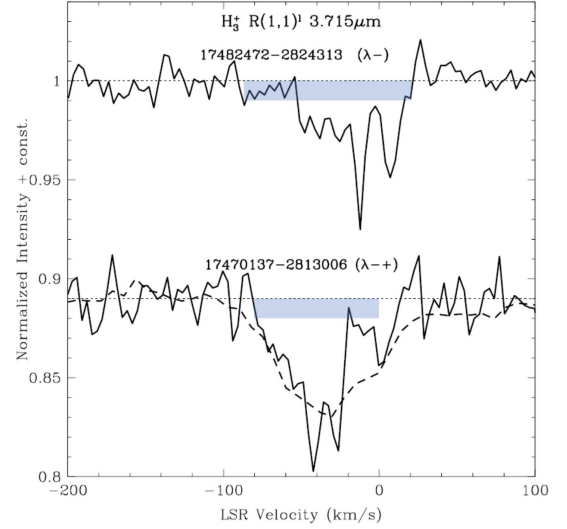


**Figure 8.** The velocity profiles of the  $R(1,1)^l$  line observed toward the  $\lambda-$  and  $\lambda-+$ . Both spectra were recorded by the Phoenix Spectrometer at the Gemini South Observatory. The low resolution dotted spectrum in the lower trace was recorded by the GNIRS spectrometer at the Gemini South Observatory. Shaded rectangles indicate the extents of the warm diffuse CMZ gas (see Section 4.5).

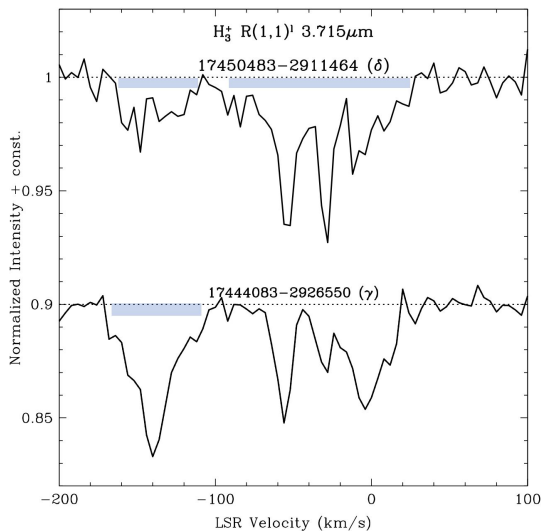
as  $-90 \text{ km s}^{-1}$ . Absorption by dense gas in the foreground spiral arms may be present, but the broad  $R(3,3)^l$  line profile clearly demonstrates the existence of warm gas over its wide range of absorption velocities.

The higher-resolution and lower-resolution  $R(1,1)^l$  spectra toward Star  $\lambda-+$  (lower trace) are generally consistent with one another. Both spectra reveal an absorption trough starting at  $\sim -80 \text{ km s}^{-1}$ . Although it is likely that there is contamination of the profile by foreground dense spiral arm gas at  $\sim -45 \text{ km s}^{-1}$  and  $-25 \text{ km s}^{-1}$ , the trough may extend to  $0 \text{ km s}^{-1}$ .

Thus, the velocity extents of the troughs toward both of these stars are somewhat uncertain. However, the key conclusion from these spectra is that the absorptions by warm diffuse CMZ gas in these easternmost stars do not extend to the highest negative velocities seen toward each of the other eastern stars closer to the Central Cluster.

#### 4.6. Stars Between the Central Cluster and the Western Edge of the CMZ : $\delta$ and $\gamma$

We now consider the spectra of stars to the west of the Central Cluster that surrounds Sgr A\*. Compared to the eastern side of the CMZ, fewer suitable stars are available Geballe et al. (2019a). Several of them were found to exhibit little or no absorption due to  $\text{H}_3^+$ , indicating that they are not deeply embedded in the CMZ (see footnote for Table 2 Paper I). However, the spectra of  $\text{H}_3^+$  toward two stars located between the center and the western edge and three stars that are very close to the western edge provide important information on the extent and kinematics of the warm diffuse gas in the CMZ.



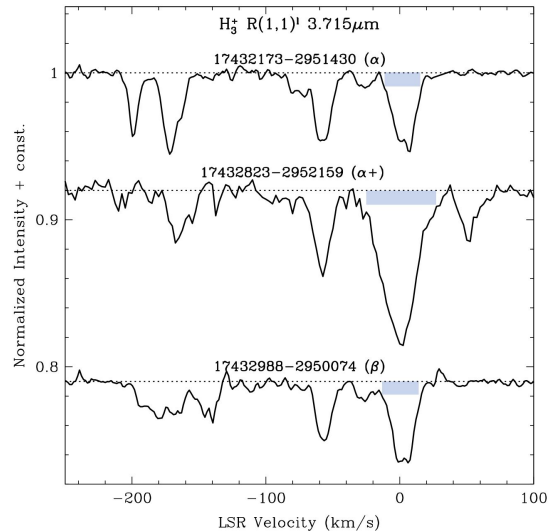
**Figure 9.** The velocity profiles of the  $R(1,1)^l$  line observed toward the stars  $\gamma$  and  $\delta$ . Both spectra were recorded by the Phoenix Spectrometer in the Gemini South Observatory. Shaded rectangles indicate the extents of the warm diffuse CMZ gas (see Section 4.6).

Figure 9 contains the spectra of the  $R(1,1)^l$  line towards the two intermediate western stars. Star  $\delta$  (upper trace) is located some 30 pc from Sgr A\*, at the same distance from it as is the Quintuplet Cluster on the opposite side. Like the stars in that cluster, its spectrum contains an extensive absorption trough, from  $\sim -160 \text{ km s}^{-1}$  to  $\sim 20 \text{ km s}^{-1}$ , albeit with narrow gap in the absorption from  $-110 \text{ km s}^{-1}$  to  $\sim -90 \text{ km s}^{-1}$ .

The  $R(1,1)^l$  velocity profile toward Star  $\gamma$  (Figure 9, lower trace), in the Sgr C complex located  $\sim 70$  pc to the west of Sgr A\* and thus approximately midway between the center and the western edge of the CMZ, is unique among all of the observed spectra in that it is entirely highly blueshifted, extending from  $-165 \text{ km s}^{-1}$  to  $-110 \text{ km s}^{-1}$ , with no trough extending to less negative velocities. The same broad absorption is also present in the spectrum of the  $R(3,3)^l$  line (Paper I, Fig. 7). The absorption in the  $R(1,1)^l$  lines has a sharp peak centered at  $-136 \text{ km s}^{-1}$ . The triangular profile of the  $R(1,1)^l$  absorption line is reminiscent of the OH radio absorption line in Fig. 2 of Bolton et al. (1964b). Although the CO spectra on this sightline show narrow absorption lines centered at  $-136 \text{ km s}^{-1}$ , they are rather weak; moreover there is no absorption in the  $R(2,2)^l$  line of  $\text{H}_3^+$  (see Figures 6 and 8 and Table 3 of Paper I). Therefore, although the sharp  $R(1,1)^l$  absorption peak at  $-136 \text{ km s}^{-1}$  may be partly due to the contribution of a dense cloud, the bulk of the absorption profile must be due to  $\text{H}_3^+$  in the diffuse gas of the CMZ. The lack of an absorption trough extending from  $-90 \text{ km s}^{-1}$  to less negative velocities is discussed further in Section 5.

#### 4.7. Stars at the Western Edge of the CMZ: $\alpha$ , $\alpha+$ , and $\beta$

Velocity profiles of the  $R(1,1)^l$  line of  $\text{H}_3^+$  toward three bright stars,  $\alpha$ ,  $\alpha+$ , and  $\beta$  at the western edge of the CMZ and close to the radio complex Sgr E are shown in Figure 10. They, together with spectra of the  $R(3,3)^l$  line and overtone



**Figure 10.** Velocity profiles of the  $R(1,1)^l$  line observed toward three stars at the western edge of the CMZ. All spectra were recorded by the Phoenix Spectrometer at the Gemini South Observatory. Shaded rectangles indicate the extents of the warm diffuse CMZ gas (see Section 4.7).

CO lines toward them presented in Geballe & Oka (2010), Goto et al. (2011), and in Paper I, have played an essential role in our overall understanding of dynamics and morphology of the CMZ warm and diffuse gas.

None of the spectra of Stars  $\alpha$ ,  $\alpha+$ , and  $\beta$  contains the broad absorption troughs that are so characteristic of almost all of the spectra toward stars that are not on the edges of the CMZ. Instead each of these stars contains three fairly narrow absorption features at negative velocities, and a strong absorption centered at  $0 \text{ km s}^{-1}$ . This last absorption component, highly important in understanding the kinematics of the warm and diffuse gas throughout the CMZ, is discussed following descriptions of the other absorption features.

##### 4.7.1. Absorption by localized dense clouds in the CMZ

The two most negative absorption velocities, at  $\sim -205 \text{ km s}^{-1}$  and  $\sim -170 \text{ km s}^{-1}$  (with some variation from one sightline to another) are seen toward all three stars. They match the velocities of two high velocity dense clouds previously observed by Liszt (1992) in  $^{13}\text{CO}$  (see the  $(l, v)$  diagram of his Fig. 3). They also match absorption velocities in spectra of overtone CO lines toward some of these sources (Geballe & Oka 2010; Paper I). In addition, emission at these velocities is also seen in far-infrared emission lines of C II and N II in this region (Langer et al. 2015), which must arise in diffuse gas associated with the dense clouds. A third strong negative velocity absorption in the  $\text{H}_3^+$  spectra, near  $-60 \text{ km s}^{-1}$ , is due to foreground dense gas in the 3 kpc spiral arm. All of these dense clouds are of minor interest for this paper and are not discussed further. In addition to them, the  $R(1,1)^l$  spectrum toward Star  $\alpha+$  (Figure 10, middle trace) contains a narrow absorption centered

at  $+51 \text{ km s}^{-1}$ , not present in the spectra of the other two stars.

All of the absorptions at negative velocities are strongly present in spectra of the overtone CO lines (Oka et al. (2019) and unpublished data), further demonstrating that the clouds producing them are dense. The presence of weak absorption in the  $R(3,3)^l$  line at  $\sim -205 \text{ km s}^{-1}$  and  $\sim -170 \text{ km s}^{-1}$  toward stars  $\alpha$  and  $\alpha+$  (see Figure 7 of Paper I) shows that the temperatures in these dense clouds are higher than in clouds in the Galactic disk, but are lower than 200 K in the diffuse gas that permeates the CMZ. Toward star  $\beta$  the  $R(3,3)^l$  high velocity absorption features are stronger relative to those in the  $R(1,1)^l$  profile, indicating somewhat higher temperatures in those parts of the high velocity clouds.

Absorption by the  $+51 \text{ km s}^{-1}$  cloud in the  $R(3,3)^l$  line is completely absent (Paper I, Fig. 7), demonstrating that the temperature of that cloud is significantly below the mean temperature of the diffuse gas in the CMZ. Although the  $+51 \text{ km s}^{-1}$  cloud probably lies within the CMZ we are uncertain of its location.

#### 4.7.2. The Absorptions near $0 \text{ km s}^{-1}$

We now turn to the unusually strong absorption features at  $0 \text{ km s}^{-1}$ , which have full widths at zero intensity ranging from 30 to  $50 \text{ km s}^{-1}$  toward stars  $\alpha$ ,  $\alpha+$ , and  $\beta$ . This absorption feature toward Star  $\alpha+$  in Figure 10 is the deepest single interstellar absorption feature in all  $\text{H}_3^+$  spectra observed to date on any sightline. Toward Star  $\alpha+$  and Star  $\beta$ , absorption by CO overtone band lines is observed near  $0 \text{ km s}^{-1}$ , implying that dense gas in the local arm contributes to the absorption in the  $R(1,1)^l$  line toward these two stars. However, because strong absorption at  $0 \text{ km s}^{-1}$  is present in the  $R(3,3)^l$  line toward all three stars (Fig. 7 of Paper I), it is clear that large column densities of warm diffuse CMZ gas at very low radial velocities, are also present on these two sightlines.

Surprisingly, no absorption near  $0 \text{ km s}^{-1}$  in the overtone band lines of CO is detected toward Star  $\alpha$  (Geballe & Oka 2010, see also Paper I). Thus there are no dense clouds in the local arm on the sightline toward this star to contaminate the spectrum of the  $R(1,1)^l$  line at low radial velocities. Diffuse gas in the local spiral arm could be present on this sightline and the  $\text{H}_3^+$  it might contain could produce an absorption feature at low velocity. However, the strong absorption in the  $R(3,3)^l$  line at this velocity shows that the deep absorption at  $0 \text{ km s}^{-1}$  in the  $R(1,1)^l$  line must be produced largely, if not entirely by warm  $\text{H}_3^+$  within the CMZ.

In summary, although in the central part of the CMZ the absorption by  $\text{H}_3^+$  in the warm and diffuse gas exists over a wide range of blueshifted radial velocities as high as  $\sim -150 \text{ km s}^{-1}$ , at the western edge of the CMZ the warm diffuse gas exists only over a narrow range of radial velocities close to  $0 \text{ km s}^{-1}$ .

## 5. DYNAMICS AND MORPHOLOGY

It was postulated in Paper I, but not demonstrated in detail, that the warm diffuse gas in the CMZ is undergoing a radial

expansion that originated near the center of the CMZ. In this section we examine that proposition more thoroughly, drawing upon the velocity profiles of the  $R(1,1)^l$  line of  $\text{H}_3^+$  presented in Section 4. We also compare our results to the earlier studies of the motion, morphology, and physical properties of the EMR by Kaifu, Kato, & Iguchi (1972) and Scoville (1972).

### 5.1. The data

The Galactic longitudes of the stars and ranges of radial velocities in which the warm diffuse gas is present, based on the spectra of the  $R(1,1)^l$  line of  $\text{H}_3^+$  presented in Section 4, are summarized in Table 1. Most of the sightlines contain broad blueshifted “troughs” of absorption by this gas. Most of these troughs have one edge at large negative velocity, well in excess of  $-100 \text{ km s}^{-1}$ , and the other edge at a velocity near zero. There are some variations, however. The troughs of three stars (NHS 21,  $\delta$  and  $\theta$ ) are noncontinuous, but contain narrow gaps, which may indicate the existence of voids of the warm and diffuse gas in parts of their sightlines or simply non-continuous distributions of velocities. For some other sightlines, the edge of the trough near  $0 \text{ km s}^{-1}$  could not be clearly located, because the trough merges with absorption by warm dense gas likely located in the CND (GCIRS 3 and GCIRS 1W) and/or overlaps with strong foreground absorption by cold gas in the local arm, as discussed in Section 4. For those stars the upper limits to the troughs are shown as  $\sim 0 \text{ km s}^{-1}$  in Table 1. For others the trough extends slightly to positive radial velocities.

For four stars broad troughs are missing and the absorptions by warm diffuse gas are narrow. For the three stars at the western edge of the CMZ,  $\alpha$ ,  $\alpha+$ , and  $\beta$ , this is understandable in our interpretation that their sightlines are perpendicular to the motion of the gas (Section 5.2.). Star  $\gamma$  located midway between the center of the CMZ and its western edge, shows only warm diffuse gas at high negative velocities. In this case the explanation may be that this star is located near the front surface of the CMZ, which, as discussed in Section 5.2, is expanding radially at high velocity.

Finally, for Star  $\iota$ , the sightline which intersects the Sgr B molecular cloud complex, unlike any of the other sightlines the broad absorption seen toward it extends to high positive velocities. Because strong absorption at these velocities is also present in spectra of the overtone CO lines (Figure 7), much of the warm gas in which these absorptions arise must be dense and be associated with Sgr B. However, as noted in Section 4.4, warm diffuse gas is clearly present at high negative velocities and may extend to very low negative velocities. We conclude that this gas is in the CMZ, but is in front of Sgr B and is not associated with it.

### 5.2. The $(l, v)$ diagram of the warm diffuse CMZ gas

The data in Table 1 are plotted in the  $(l, v)$  diagram shown in Figure 11. The green semicircle of radius  $1^\circ$  and  $150 \text{ km s}^{-1}$  indicates the outer edge of the warm ( $T \sim 200 \text{ K}$ ) and diffuse ( $n \sim 50 \text{ cm}^{-3}$ ) CMZ gas, assumed to be

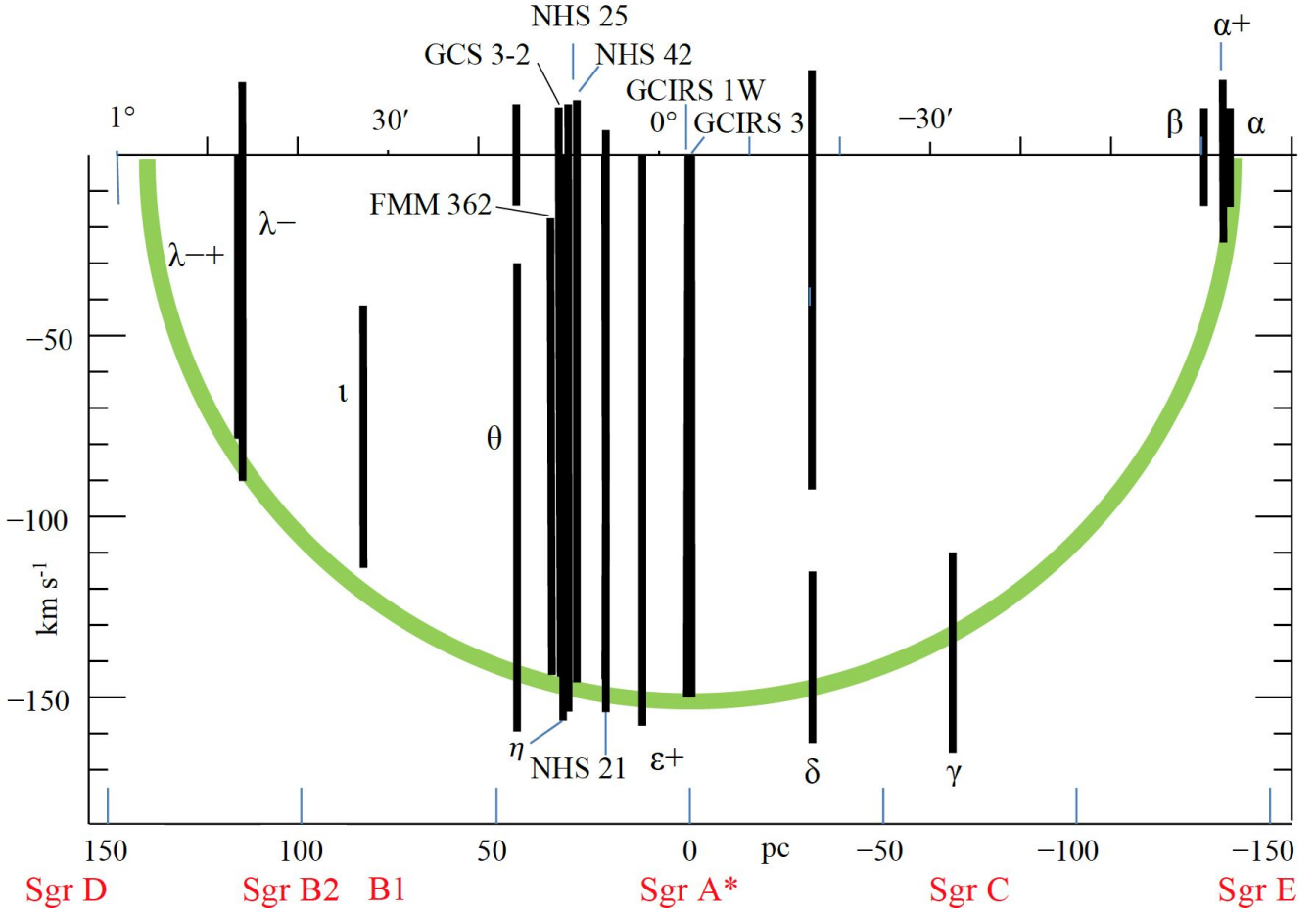


**Figure 11.** The  $(l, v)$  diagram for the observed velocity profiles of the  $\text{H}_3^+$  toward 18 stars, created using the data compiled in Table 1. Galactic longitude is given at top and longitudinal distance from Sgr A\* (at  $G_{\text{lon}} = -0.056^\circ$ ) in pc is at bottom. Approximate  $G_{\text{lon}}$  and distances of Sagittarius radio sources with respect to Sgr A\*: Sgr E ( $-1.079^\circ$ ,  $-143$  pc); Sgr C ( $0.571^\circ$ ;  $-72$  pc); Sgr B1 ( $0.506^\circ$ ,  $79$  pc), Sgr B2 ( $0.667^\circ$ ,  $101$  pc), and Sgr D ( $1.126^\circ$ ,  $166$  pc) are shown at bottom. The semicircle indicates the front of the expanding gas with radius  $1^\circ$  and velocity of  $150 \text{ km s}^{-1}$ . The black vertical line segments indicate the ranges of radial velocities for which absorption by warm diffuse gas is detected. Individual sightlines are labeled. For Star  $\iota$  note the discussion at the end of Section 4.4.

expanding radially at  $150 \text{ km s}^{-1}$ , approximately at the same velocity as the EMR.

As can be seen in the figure, the highest observed negative radial velocities of the warm diffuse gas match this simple model very well. The largest deviations are somewhat to the west of center, where the sightlines to Stars  $\gamma$  and  $\delta$  contain gas at moderately higher maximum negative velocities than the model. These might be explained by asymmetries in the initial ejection of the gas or in preexisting density nonuniformities in the CMZ.

The close match between the highest negative velocities in the  $\text{H}_3^+$  absorption troughs and the velocities observed in the EMR strongly indicates that the warm diffuse gas observed at the highest velocities is located at or close to the EMR, lending strong support to an interpretation of the spectra as the result of radial expansion. The warm diffuse gas observed

at lower velocities on these sightlines would then lie inside the CMZ (as is suggested by the velocity profile of Star  $\gamma$  in Figure 9). This interior gas must also be undergoing largely outward radial motion. Little or none of it is falling toward the center (a possibility that might have been expected because of the gravitational potential; see Section 6.3). If some of it were infalling, absorption would also be expected to be present over an extensive range of positive velocities. Such absorption is not observed. Finally and most critically, the considerably lower radial velocities observed toward the two stars near the eastern edge of the CMZ, and in particular the very low radial velocities and narrow velocity ranges seen on sightlines to the three stars close to the western edge of the CMZ, are key support for the radial expansion interpretation. This is because (1) radial expansion viewed at the edges of the CMZ is perpendicular to the line of sight, and (2) the

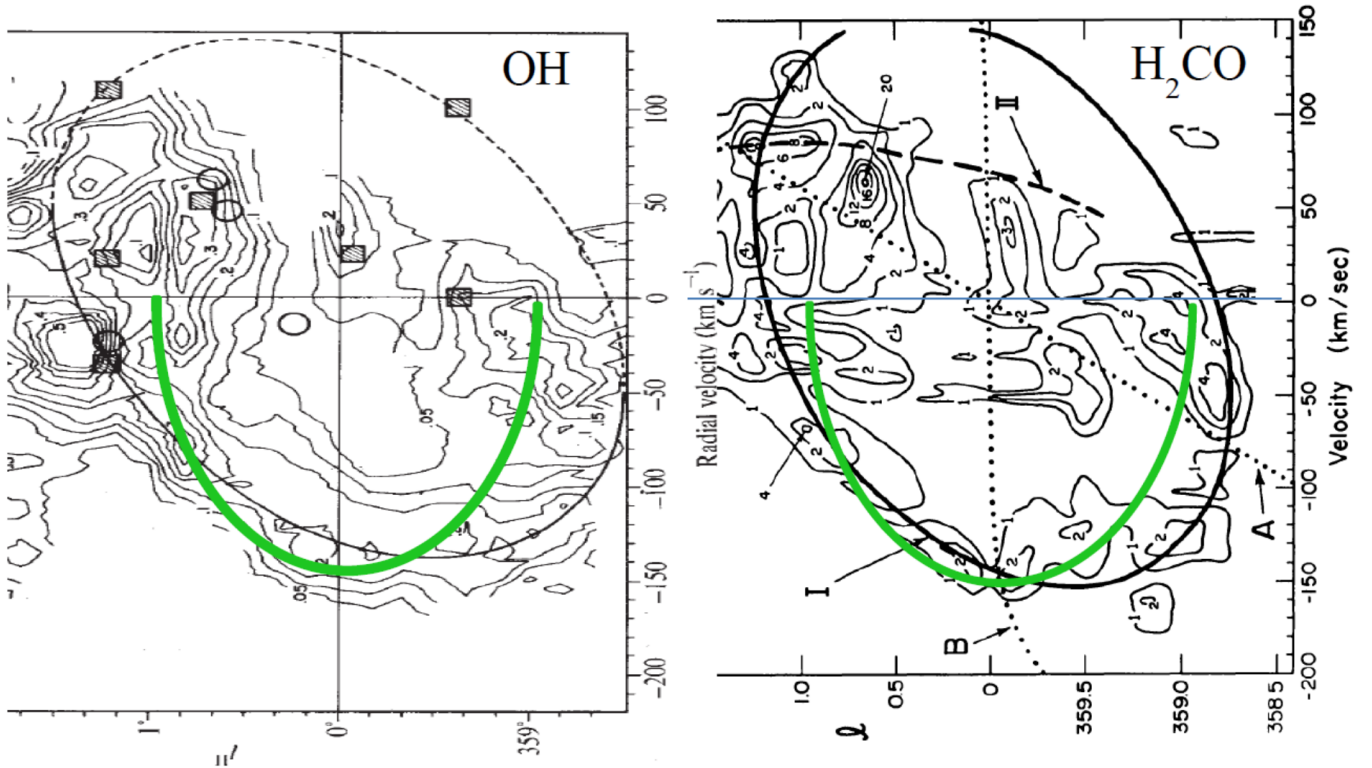


**Figure 12.** Comparisons between the  $(l, v)$  diagram of the front surface of the expanding diffuse gas obtained from  $\text{H}_3^+$  (green lines) and those of the EMR by Kaifu, Kato, & Iguchi (1972) (left panel, continuous line) and Scoville (1972) (right panel, continuous line). Kaifu et al. used the contour map of the 1667 MHz OH absorption reported by McGee (1970) to draw the front half of the EMR and two 1.3 cm  $\text{NH}_3$  emission lines (shaded rectangles) to fit the back part of the EMR (left panel, dashed line). Scoville’s  $(l, v)$  diagram is based on an absorption line of  $\text{H}_2\text{CO}$ .

strengths of these absorptions imply column lengths of tens of pc (Paper I).

Note that apart from the velocity profile toward Star  $\iota$ , none of the spectra of  $\text{H}_3^+$  lines reveals warm diffuse highly redshifted gas. In a symmetric radial expansion such gas should be present if the background stars are spread throughout the front and rear halves of the CMZ. As discussed in Paper I, we believe that the absence of redshifted  $\text{H}_3^+$  is a selection effect, largely the result of the brightness constraint imposed in order to obtain spectra of  $\text{H}_3^+$  of sufficient quality. The existence of highly redshifted gas in the EMR is demonstrated by the radio observations of Kaifu, Iguchi, & Kato (1974) and Scoville (1972).

### 5.3. Comparison with $(l, v)$ diagrams of Kaifu et al. and Scoville

In Figure 12 the  $(l, v)$  diagrams of the EMR obtained from radio absorption spectra of OH by Kaifu, Kato, & Iguchi (1972) and of  $\text{H}_2\text{CO}$  by Scoville (1972) are compared with the simple  $(l, v)$  diagram based on the highest observed velocities of  $\text{H}_3^+$  (Figure 11). In view of the simplicity of the fit to the  $\text{H}_3^+$  data, based on widely spaced data points, and the low resolution of the radio data, the infrared and radio

diagrams are in good agreement. The  $(l, v)$  diagrams and properties of the EMR are discussed in more detail below.

#### 5.3.1. Dense or diffuse gas

While the expanding gas observed in  $\text{H}_3^+$  has a low mean density ( $n \sim 50 \text{ cm}^{-3}$ , Paper I), both Kaifu, Kato, & Iguchi (1972) and Scoville (1972) reported the gas forming the EMR to be dense ( $n \geq 10^3 \text{ cm}^{-3}$ ). Kaifu et al. used the  $(l, v)$  diagram of the strongest hyperfine component of the  $\Lambda = 3/2$  OH  $\Lambda$ -doubling transition at 1667.36 MHz reported by McGee (1970) to draw the front half of the EMR and used observations of radio  $\text{NH}_3$  emission lines at two locations to aid in filling in the rear half. From the  $\text{NH}_3$  emission they concluded the gas density in the EMR to be  $10^3$ – $10^4 \text{ cm}^{-3}$ . The two data points of  $\text{NH}_3$  (see Figure 12 left) may well be coincident with the EMR, but we believe that determining the density of the EMR from  $\text{NH}_3$  emission is not justified. The OH lines are more likely to result from the absorption of scattered microwave radiation from the Galactic center than from the cosmic microwave background. Because of the large beam size ( $12''.2$  at the 210 ft Parkes telescope, McGee 1970) detailed analysis of the OH data is a complex and nearly impossible task. Nevertheless, that the 18 cm line

is in absorption suggests much lower densities than assumed by Kaifu, Kato, & Iguchi (1972).

The  $(l, v)$  diagram proposed by Scoville (1972) is based on the radio absorption spectrum of the  $\text{H}_2\text{CO } 1_{10} \leftarrow 1_{11}$   $K$ -doubling transition at 4829.73 MHz (6.2 cm). However, the density of the EMR,  $n_{\text{H}_2} > 10^3 \text{ cm}^{-3}$  adopted by him is based on the  $J = 1 \rightarrow 0$  CO line emission. CO emission in this line is ubiquitous in the CMZ and we believe that an estimation of the density of gas in the EMR from it is not justified. The excitation of the energy levels of the  $K$ -doublet of  $\text{H}_2\text{CO}$  is a complex problem (Townes & Cheung 1969; Oka 1970) and the determination of cloud density based on its absorption spectrum is even more complicated than that for OH.

From these considerations and the good agreement of the  $(l, v)$  diagram for the front of the expanding gas and the EMR, we believe that the gas in the EMR, which is located at the outer edge of the CMZ, has similar properties to the diffuse gas observed in  $\text{H}_3^+$  throughout the CMZ and that they are physically connected. We note that in the spectra published in Paper I there are a few sightlines where weak absorption by overtone lines of CO is present at negative velocities near  $-150 \text{ km s}^{-1}$ , suggesting that there is some dense molecular gas in the CMZ that is near or part of the EMR. That would not be surprising, as high velocity gas within the CMZ should be impacting the EMR and driving it outward. In addition the EMR must be colliding with and accumulating gas from the external interstellar medium. Both of these processes will tend to increase the density where the impacts are occurring and thus it is conceivable that the EMR contains regions of dense molecular gas. However, based on spectroscopy of  $\text{H}_3^+$  and the CO overtone band lines, these regions appear to be few and far between. Reducing the density of the gas in the EMR by 1–2 order of magnitude, as suggested above, brings the kinetic energy of the EMR reported by Kaifu, Kato, & Iguchi (1972) ( $10^{55}$ – $10^{56}$  erg) and Scoville (1972) ( $> 6 \times 10^{53}$  erg) into better agreement with the kinetic energy of the EMS ( $2 \times 10^{54}$  erg) estimated by Sofue (1995b).

### 5.3.2. Ring, filled disk, or both?

Both the high column densities of  $\text{H}_3^+$  and the broad absorption troughs of its  $R(1,1)^l$  and  $R(3,3)^l$  lines on many sightlines, as illustrated in Figure 11, lead to the conclusion in Paper I that warm diffuse gas fills much of the CMZ. In contrast, the  $(l, v)$  diagrams of OH and  $\text{H}_2\text{CO}$  indicate rings of molecular gas with a void in the center. Although quantitative analysis is complicated for OH and  $\text{H}_2\text{CO}$  and is beyond the scope of this paper, we suspect that the differences in the distributions of these species are related to differences in their chemistries. The molecular ion  $\text{H}_3^+$ , being extremely active chemically, has a very short lifetime in the CMZ, where electrons abound due to rapid ionization of H and  $\text{H}_2$  by the high cosmic ray flux. From the high rate constant for dissociative recombination  $\sim 10^{-7} \text{ cm}^3 \text{ s}^{-1}$  at  $T \sim 200 \text{ K}$  (McCall et al. 2004) and the high electron number density  $n_e \sim 0.33 \text{ cm}^{-3}$  (Paper I), the lifetime of an  $\text{H}_3^+$  ion in the CMZ is estimated

to be on the order of years. Thus,  $\text{H}_3^+$  is constantly being created and destroyed throughout the CMZ and should be distributed more or less uniformly in it.

On the other hand, OH and  $\text{H}_2\text{CO}$  have much longer lives and their distributions are more specific to the environment. They have 1000 times higher rates of photodissociation by FUV than  $\text{H}_3^+$  (van Dishoeck 1988; Heays, Bosman, & van Dishoeck 2017). The UV field has been estimated to be 1,000 times higher in the CMZ than in the solar neighborhood (Rodríguez-Fernández et al. 2004). In the CMZ most of the stars, including many of the hottest and most luminous ones, e.g., those in the Central, Quintuplet, and Arches clusters, are centrally concentrated. Hence, the UV intensity should decrease with distance from the center beyond  $\sim 30 \text{ pc}$ , apart from local effects. This may result in the abundances of OH and  $\text{H}_2\text{CO}$  increasing with increasing distance from the center, showing peaks at the EMR, and thus appearing as rings. Readers are also referred to the  $(l, v)$  diagram of OH absorption in Fig. 9 of Cohen & Few (1976), where the filling inside the EMR for this molecule seems somewhat more uniform than in Figure 12 (left panel).

### 5.3.3. Rotation?

While the  $(l, v)$  diagram of  $\text{H}_3^+$  is interpreted as due to purely expanding gas in this paper, both Kaifu, Kato, & Iguchi (1972) and Scoville (1972) interpreted their  $(l, v)$  diagrams as indicating an *expanding and rotating ring* with expansion and rotational velocities  $130 \pm 5 \text{ km s}^{-1}$  and  $50 \pm 20 \text{ km s}^{-1}$ , and  $145 \text{ km s}^{-1}$  and  $50 \text{ km s}^{-1}$ , respectively. The difference between their estimates and ours stems from the difference in symmetries with respect to  $G_{\text{lon}}$ . In Figure 12, the (half) ellipse drawn as showing the front of the expanding gas based on spectra of  $\text{H}_3^+$  is symmetric with respect to longitudinal distance from Sgr A\* while the elliptical fits to the  $(l, v)$  diagrams of OH and  $\text{H}_2\text{CO}$  are not. However, in our examination of the contour plots of these two molecules without the elliptical fits, we do not see convincing evidence for this asymmetry.

The essential difference between the half ellipse obtained from  $\text{H}_3^+$  and the ellipses derived for the EMR is that while the former gives zero radial velocity at the westmost edge, the latter extend farther to negative velocities to the west because of the asymmetry with respect to  $G_{\text{lon}}$ . If the latter were correct, the OH ellipse implies that an absorption trough of  $\text{H}_3^+$  would be present from 0 to  $\sim -80 \text{ km s}^{-1}$  in the spectra toward Stars  $\alpha$ ,  $\alpha+$ , and  $\beta$ ; the  $\text{H}_2\text{CO}$  ellipse would predict an absorption trough from 0 to  $\sim -120 \text{ km s}^{-1}$ . Such troughs are not seen in  $\text{H}_3^+$ , demonstrating that the asymmetry does not exist and that the EMR is not rotating.

## 6. ORIGIN AND FUTURE OF THE RADIAL EXPANDING GAS

The concerted gas motion away from the center discovered by Kaifu, Kato, & Iguchi (1972) and Scoville (1972) and confirmed in this paper must be either the result of a large accumulation of energetic stellar events or the result of one or more much more energetic expulsion events near the

center in the recent past, possibly associated with Sgr A\*. In the following sections we attempt to constrain the possible explanations of the observed radial expansion and to predict the future of the CMZ's diffuse gas.

### 6.1. Momentum considerations

Using the estimated mean density and filling factor of the warm diffuse gas, the total mass of the warm diffuse expanding gas was calculated in Paper I to be  $6 \times 10^6 M_\odot$  (see Paper I, Table 7). For comparison, the mass of the EMR had been estimated to be  $3 \times 10^6 M_\odot$  by [Scoville \(1972\)](#) and  $1 \times 10^7 M_\odot$  by [Kaifu, Iguchi, & Kato \(1974\)](#). However, as discussed in Section 5.2.1 we believe their estimates of density are too high by 1–2 orders of magnitude.

We estimate that the current radial momentum of the CMZ's warm diffuse gas to be approximately  $5 \times 10^8 M_\odot \text{ km s}^{-1}$  (using a mean gas velocity  $v$  of  $75 \text{ km s}^{-1}$ ). This is comparable to that generated by approximately  $10^4$  core-collapse supernovae, assuming that each supernova ejects  $10 M_\odot$  at an average speed of  $3,000 \text{ km s}^{-1}$ . Note that this estimate is a lower limit, because the radial momentum of the CMZ gas decreases with time as a consequence of the gravitational attraction by the enclosed mass, as discussed below. The current kinetic energy of this gas (assuming a mean  $v^2$  of  $10^4 \text{ km}^2 \text{ s}^{-2}$ ) is  $\sim 5 \times 10^{53} \text{ erg}$ .

This decrease in radial momentum is significant. A crude characteristic expansion time of the CMZ gas, assuming the current maximum velocity of  $150 \text{ km s}^{-1}$  and the CMZ radius of  $150 \text{ pc}$ , is  $\sim 1 \times 10^6 \text{ yr}$ . Using Fig. 14 of [Sofue \(2013\)](#), [Geballe, Oka, & Goto \(2019b\)](#) estimate that the deceleration due to gravity from a distance of  $30 \text{ pc}$  from Sgr A\* to the edge of the CMZ at  $r = 150 \text{ pc}$  is  $\sim 1 \times 10^{-6} \text{ cm s}^{-2}$ . Because of the gravitational potential, in one million years gas ejected into the CMZ near its center would have decelerated by a few hundred  $\text{km s}^{-1}$  from an initially much higher velocity than the maximum velocity of  $150 \text{ km s}^{-1}$  presently observed. This implies that the current radial momentum in the outflowing gas is considerably less than half of what it was one million years ago. Using a shorter characteristic time to account for the deceleration, would still require a much higher initial radial momentum than the above value.

The supernova rate in the CMZ has been variously estimated to be  $(1-10) \times 10^{-4} \text{ yr}^{-1}$  ([Crocker et al. 2011](#); [Zubovas, Wynn, & Gualandris 2013](#)). Even the highest estimated rate would fall short of generating the current radial momentum by an order of magnitude in one million years, and by more if the larger initial radial momentum required by a shorter characteristic time are used.

The radial momentum of the CMZ gas also exceeds, by a much larger factor, the total radial momentum generated by winds of all of the several hundred massive stars of the three massive clusters (Central, the Quintuplet, and the Arches) in the central  $30 \text{ pc}$  of the CMZ during their few million year lifetimes. Assuming each star ejects  $10 M_\odot$  of its mass at  $1,000 \text{ km s}^{-1}$  before exploding,  $3 \times 10^4$  such stars would be required to account for the observed radial momentum, two orders of magnitude more than are currently present.

Although estimates are highly uncertain, normal red giants might have contributed an appreciable fraction of the current mass and radial momentum of the CMZ, but they cannot be responsible for the high velocities that are observed for much of this gas.

The births of the above three massive clusters, must have been accompanied with ejection of large mass with high velocities. Their time of formation 4.8 million years ago for the Quintuplet Cluster (e.g. [Schneider et al. 2014](#)) and 2.5 million years ago for the Arches Cluster (e.g. [Espinoza, Selman, & Melnick 2009](#)), however, are much greater than the characteristic expansion time of the CMZ and EMR gases.

### 6.2. Past explosive events

In view of the above discussion, one must consider whether the expanding gas was produced by some other means. Possibly, the gas is the aftermath of one or more explosive events in the nucleus associated with the supermassive black hole. In view of the above estimates of the characteristic time such events would have occurred several hundred thousand to one million years ago. Both [Kaifu, Kato, & Iguchi \(1972\)](#) and [Scoville \(1972\)](#) invoked such events to account for the EMR.

Expulsion events have been previously suggested by many authors. In a series of papers on north and south radio spurs beginning with [Sofue \(1973\)](#), Sofue proposed that the spurs are results of star bursts near the GC, contrary to the consensus at the time that they are supernova remnants in the vicinity of the solar system. His magnetohydrodynamic wave calculation ([Sofue 1976, 1977](#)) based on [Uchida \(1970\)](#) provided support for the idea. Observations of radio continuum emission by Sofue and Handa (1984) revealed a giant Q-shaped radio loop, the Galactic center lobe (GCL). This result together with X-ray maps by [McCammon et al. \(1983\)](#) and [McCammon & Sanders \(1990\)](#) led [Sofue \(1994\)](#) to propose that a giant explosion at the GC, of energy  $3 \times 10^{56} \text{ erg}$ , occurred 15 million years ago. From further studies of X-rays via ROSAT all-sky maps ([Snowden et al. 1997](#)) and adiabatic shock wave calculations based on [Sakashita \(1971\)](#) and [Möllenhoff \(1976\)](#), [Sofue \(2000\)](#) proposed a bipolar hyper-shell model for the ejecta. This model can be considered as anticipating the discovery of the bipolar  $\gamma$ -ray Fermi Bubbles ([Dobler et al. 2010](#); [Su, Slatyer, & Finkbeiner 2010](#)). Although estimated ages of the Fermi Bubbles vary by large factors, they generally suggest an explosion at the GC about 10 million years ago. The relation between microwave lobes, X-ray and  $\gamma$ -ray maps, all indicating explosive events in the GC, are discussed in [Kataoka et al. \(2018\)](#) and [Sofue \(2019\)](#). These events appear to be more than 10 times older and possessing much higher energy than could account for the current state of the warm diffuse CMZ gas reported here.

The  $430 \text{ pc}$  bipolar radio bubble recently detected by MeerKAT ([Heywood et al. 2019](#)) indicates explosive events of much smaller scale both in time (a few million years) and total energy ( $7 \times 10^{52} \text{ erg}$ ). However, the gas velocity of  $30 \text{ km s}^{-1}$  ([Law et al. 2009](#)) used for estimating the time may well be much larger. If so the time since the event occurred is under one million years in agreement with estimate in this

paper. Indeed the value of “a few times  $10^5$ – $10^6$  years ago” given by [Yusf-Zadeh & Wardle \(2019\)](#) contains an estimate of somewhat less than 1 million years, well within our proposed range of ages. The energy of the expanding CMZ gas of  $5 \times 10^{53}$  erg is an order of magnitude higher than the estimated energy of the radio lobe. Together with the question of why the explosion energy is in-plane, further discussion of these issues is left for the future. From the agreement of the ages of these events, it is possible that the expanding gas observed in  $\text{H}_3^+$  and the MeerKAT radio bubble were caused by the same explosive event.

### 6.3. Deceleration and future infall of the CMZ gas

Currently, there is no evidence that at the present time the expanding diffuse gas that the CMZ contains is being actively driven outward. It is thus of interest to consider the effect of gravity on the gas. The deceleration by the gravitational force from the enclosed mass of the Galaxy ([Sofue 2013](#), Fig. 14) increases rapidly from 30 pc from the center inward, but is fairly constant at approximately  $1 \times 10^{-6} \text{ cm s}^{-2}$  between 30 pc and 150 pc from Sgr A\*. As discussed earlier, the decrease in radial velocity over the characteristic time of  $1 \times 10^6$  yr for the expanding gas, is then approximately  $300 \text{ km s}^{-1}$ . This is roughly twice the observed current maximum expansion velocity of the warm diffuse gas. If the characteristic time is roughly half of the above value, due to taking into account the previous deceleration of the gas, the decrease in velocity is equal to the current maximum expansion velocity (See Appendix for a formal calculation).

As can be seen in Fig. 14 of [Sofue \(2013\)](#), beyond the radius of the CMZ, the enclosed mass increases slightly less rapidly with distance from the center than at smaller radii. However at 300 pc the deceleration due to gravity has only decreased to two-thirds the above value. Thus it is clear that the expanding gas in the EMR and CMZ will not escape from the Galactic center. A more quantitative calculation given in the Appendix leads us to the same conclusion.

The above considerations suggest the following scenario. The expansion of highest velocity warm diffuse gas will end in roughly  $5 \times 10^5$  yr. Outward motion of the lower velocity gas in the interior of the CMZ will end sooner. Warm diffuse gas will begin to fall back towards the center. Gas densities in the inner part of the CMZ will increase and new episodes of star formation within the CMZ as well as outbursts associated with gas accreting onto Sgr A\* could follow. These events could begin to occur after an additional few hundred thousand years.

Note that this scenario ignores any role played by dense molecular clouds, whose total mass has been estimated to be several times that of the diffuse CMZ gas ([Sofue 2017](#)). Because the filling factor in the CMZ of the dense gas is believed to be much smaller than that of the diffuse gas, the evolution of the diffuse gas may be largely independent of the dense clouds, unless one of the latter falls into the center at an earlier time.

## 7. SUMMARY AND CONCLUSIONS

We have obtained velocity profiles of the  $R(1,1)^l$  line of  $\text{H}_3^+$  at  $3.7 \mu\text{m}$  toward 29 stars whose sightlines are toward the CMZ of the Galaxy and extend in longitude nearly fully across the CMZ; we present 18 of them in this paper. These 18 stars are sufficiently deeply embedded in the CMZ that strong absorptions are observed in the  $R(1,1)^l$  line, implying long columns of  $\text{H}_3^+$ . As discussed in Paper I, they, together with supporting observations of other lines of  $\text{H}_3^+$ , imply that warm ( $\sim 200 \text{ K}$ ) and diffuse ( $\sim 50 \text{ cm}^{-3}$ ) gas fills the majority of the volume of the CMZ.

The absorption lines of  $\text{H}_3^+$  seen toward those stars in the central part of the CMZ are broad and blueshifted, extending from  $\sim -150 \text{ km s}^{-1}$  to  $\sim 0 \text{ km s}^{-1}$ . Toward most of the stars the absorptions are continuous and form troughs, while toward a few they are discontinuous indicating patchy voids in the diffuse gas. In general the maximum (negative) velocities of the line profiles decrease with distance of the sightline from the center of the CMZ. Sightlines at the western edge of the CMZ show narrow absorptions centered at  $0 \text{ km s}^{-1}$ . No sightlines are available at the eastern edge but those closest to it have considerably narrower absorption troughs and considerably lower maximum (negative) absorption velocities than the lines on more centrally located sightlines.

The  $(l, v)$  diagram of these line profiles are well fitted by a semicircle whose radius corresponds to the maximum velocity of  $150 \text{ km s}^{-1}$  and whose linear dimension is that of the CMZ. The diagram implies that the warm diffuse gas is expanding from an origin near the center of the CMZ. This motion is similar to that of the Expanding Molecular Ring (EMR) discovered by [Kaifu, Kato, & Iguchi \(1972\)](#) and [Scoville \(1972\)](#), although there are three qualitative differences:

1. The EMR was originally interpreted as composed of dense ( $n > 10^3 \text{ cm}^{-3}$ ) gas while the gas probed by  $\text{H}_3^+$  is diffuse ( $n \sim 50 \text{ cm}^{-3}$ ). We believe that the density estimates of [Kaifu, Kato, & Iguchi \(1972\)](#) and [Scoville \(1972\)](#), which were not directly obtained from the observed absorption spectra of OH and  $\text{H}_2\text{CO}$ , but from emission spectra of  $\text{NH}_3$  and CO, respectively, are overestimates and that the EMR has roughly the same density as is derived from observations of  $\text{H}_3^+$ .
2. While the EMR as viewed in OH and  $\text{H}_2\text{CO}$  is a ring with a void at the center, the gas probed by  $\text{H}_3^+$  fills the CMZ. While  $\text{H}_3^+$  is easily understood as being present throughout the CMZ, the intense UV radiation field in the central part of the CMZ could account for the abundances of OH and  $\text{H}_2\text{CO}$  increasing with distance from the center and reaching maxima at the EMR.
3. The EMR was reported to have a rotational component with velocity  $\sim 50 \text{ km s}^{-1}$  both by [Kaifu, Kato, & Iguchi \(1972\)](#) and [Scoville \(1972\)](#). We believe that their arguments in support of this motion are not convincing. The observations of  $\text{H}_3^+$  toward the edges of the CMZ are unequivocal in demonstrating very little or no rotational component.

Analysis of the spectra of  $\text{H}_3^+$  allow us to infer that a face-on view of the CMZ would show it to be circular. This revives the circular face-on view of the CMZ proposed by Kaifu, Kato, & Iguchi (1972) and Scoville (1972), which fell out of favor after the paper by Binney et al. (1991). Although there is good evidence for elliptical orbits with high eccentricity on scales of a few kpc, the application of the Binney et al. theory to the CMZ, which is more than 10 times smaller and for which there is no evidence for the presence of a barred potential is not justified. We believe that the face-on views of the CMZ as an ellipse with high eccentricity, such as those in Fig. 2 of Rodríguez-Fernández et al. (2006), Fig. 21 of Bally et al. (2010), and Fig. 4 of Tsujimoto et al. (2018) are incorrect.

The observations of  $\text{H}_3^+$ , together with those of OH and  $\text{H}_2\text{CO}$  in the EMR indicate that nearly  $10^7 M_\odot$  of gas was expelled from central region of the CMZ roughly 600,000 years ago (see Appendix). The current kinetic energy and momentum in the gas greatly exceed what could be produced by supernovae and/or stellar winds, and the ejection is probably related to activity of Sgr A\*. Compared with explosions inferred from other observations like the microwave lobes (Sofue & Handa 1984), X-ray maps (McCammon & Sanders 1990; Snowden et al. 1997), and the  $\gamma$ -ray Fermi bubbles (Su, Slatyer, & Finkbeiner 2010), both the time and energy are an order of magnitude less. The time scale agrees with that of the recently discovered 430 pc microwave bubble (Heywood et al. 2019; Yusf-Zadeh & Wardle 2019; Yusef-Zadeh et al. 2019). The origin of the expansion of the diffuse gas probed by  $\text{H}_3^+$  may be the result of the same event or events that created the microwave bubble.

Due to the significant deceleration of the gas produced by the enclosed Galactic mass, it can be deduced that originally the maximum expansion velocity was considerably higher than the current value of  $\sim 150 \text{ km s}^{-1}$ . The ongoing deceleration will halt the expansion of the EMR within  $\sim 5 \times 10^5 \text{ yr}$  and may have already nearly halted the expansion of some of the diffuse gas interior to the EMR. This will result in infall of the gas (unless it is prevented by another outburst in the center), causing new episodes of star formation and violent events associated with accretion onto Sgr A\*.

## ACKNOWLEDGMENTS

We are grateful to F. Yusef-Zadeh, Y. Sofue, H. Liszt, and T. Oka for many helpful discussions over the last 20 years, as well as comments on an earlier draft of this paper. We thank N. Indriolo and M. Goto for helping to obtain and reduce some of the spectra, and M. Goto for other assistance. We also are indebted to the referee for several helpful suggestions. This paper is based in large part on observations obtained at the international Gemini Observatory (Programs GS-2003A-Q-33, GS-2008A-C-2, GS-2009A-C-6, GN-2010AQ-92, GN-2011A-Q-105, GN-2011B-Q-12, GN-2011B-Q-90, GN-2012A-Q-75, GN-2012A-Q-121, GN-2013A-Q-114, GN-2014A-Q-108, GS-2014A-Q-95, GN-2015A-Q-402, GS-2015A-Q-96, GN-2016A-Q-96, GS-2016A-Q-102, and GS-2017A-Q-95). Gemini Observatory is a program of NOIR-Lab, which is managed by the Association of Universities for Research in Astronomy (AURA) under a cooperative agreement with the National Science Foundation. on behalf of the Gemini Observatory partnership: the National Science Foundation (United States), National Research Council (Canada), Agencia Nacional de Investigación y Desarrollo (Chile), Ministerio de Ciencia, Tecnología e Innovación (Argentina), Ministério da Ciência, Tecnologia, Inovações e Comunicações (Brazil), and Korea Astronomy and Space Science Institute (Republic of Korea). We thank the staffs of the Gemini Observatory, the Very Large Telescope, the Subaru Telescope, and the United Kingdom Infrared Telescope for their support.

*Facilities:* Gemini:Gillett, Gemini:South, Subaru, UKIRT

## APPENDIX

## A. GAS UNDER CONSTANT DECELERATION

The gravitational deceleration of the spherically expanding gas in the spherically distributed mass of the CMZ is

$$\frac{d^2r}{dt^2} = -\frac{GM(r)}{r^2}, \quad (\text{A1})$$

where  $r$  is the distance from the center of expansion,  $G$  is the gravitational constant, and  $M(r)$  is the mass within the sphere of radius  $r$ . We use  $M(r)$  given in Fig. 14 of Sofue (2013) which is approximated as  $M(r) = \mu r^2$  between 30 pc  $\equiv r_0$  and 150 pc  $\equiv R$  with  $M(r_0) = 6.0 \times 10^7 M_\odot$  and  $M(R) = 1.5 \times 10^9 M_\odot$ .  $G\mu \equiv \gamma = 1.0 \times 10^{-6} \text{ cm s}^{-2}$ . For this mass distribution, the deceleration is constant between 30 pc and 150 pc,

$$\frac{d^2r}{dt^2} = \gamma, \text{ i.e., } \frac{dr}{dt} = v = v_0 \gamma t, \text{ and } r = r_0 + v_0 t \gamma \frac{t^2}{2}, \quad (\text{A2})$$

where  $v_0$  is the velocity of the gas at 30 pc and the time  $t$  is set to be 0 at 30 pc. These quadratic simultaneous equations with  $t$  and  $v_0$  as unknowns give the solution

$$t = \left[ \left( \frac{v}{\gamma} \right)^2 + \frac{2(rr_0)}{\gamma} \right]^{1/2} - \frac{v}{\gamma}, \text{ and } v_0 = v + \gamma t. \quad (\text{A3})$$

For the gas at the front of expansion with  $v = V = 150 \text{ km s}^{-1}$  and  $rr_0 = Rr_0 = 120 \text{ pc}$  the time of expansion  $T$  is calculated to be

$$T = 5.3 \times 10^5 \text{ year, and the initial velocity } v_0 = 310 \text{ km s}^{-1}, \quad (\text{A4})$$

Thus the gas at the front of the expansion had a speed of  $310 \text{ km s}^{-1}$  at 30 pc and has decelerated to  $150 \text{ km s}^{-1}$  during the expansion from 30 pc to 150 pc. The expansion from the origin to 30 pc must have happened in much shorter time than  $T$ . We thus conclude that the event which initiated the expansion of the gas occurred about  $6 \times 10^5$  years ago.

Figure 14 of Sofue (2013) indicates that the relation  $M(r) = \mu r^2$  holds approximately beyond  $r = 150 \text{ pc}$  up to 300 pc. Because of the constant deceleration in the region, the gas will reverse its velocity and fall back to the center long before it reaches 300 pc and join the inevitable inflow toward the center (Morris & Serabyn 1996).

## REFERENCES

- Athanassoula, E. 1992a, MNRAS, 259, 228  
Athanassoula, E. 1992b, MNRAS, 259, 354  
Bally, J., Stark, A. A., Wilson, R. W., & Henkel, C. 1987, ApJS, 65, 13  
Bally, J., Stark, A. A., Wilson, R. W., & Henkel, C. 1988, ApJ, 324, 223  
Bally, J., Aguirre, J., Battersby, C., et al. 2010, ApJ, 721, 137  
Bania, T. M. 1977, ApJ, 216, 381  
Becklin, E. E., & Neugebauer, G. 1975, ApJ, 200, L71  
Becklin, E. E., Matthews, K., Neugebauer, G., & Willner, S. P. 1978, ApJ, 219, 121  
Binney, J., Gerhard, O. E., Stark, A. A., Bally, J., & Uchida, K. I. 1991, MNRAS, 252, 210  
Binney, J., & Merrifield, M. 1998, Galactic Astronomy, Princeton University Press, Princeton, New Jersey  
Blitz, L., Binney, J., Lo, K. Y., Bally, J., & Ho, P. T. P. 1993, Nature, 361, 417  
Bolton, J. G., van Damme, K. J., Gardner, F. F., & Robinson, B. J. 1964a, Nature, 201, 279  
Bolton, J. G., Gardner, F. F., McGee, R. X., & Robinson, B. J. 1964b, Nature, 204, 30  
Burton, W. B., & Liszt, H. S. 1978, ApJ, 225, 815  
Cohen, R. J., & Few, R. W. 1976, MNRAS, 176, 495  
Contopoulos, G. 1975, ApJ, 201, 566  
Contopoulos, G., & Mertzaniades, C. 1977, A&A, 61, 477  
Crocker, R. M., Jones, D. I., Aharonian, F., Law, C. J., Melia, F., Oka, T., & Ott, J. 2011, MNRAS, 413, 763  
Dahmen, G., Hüttemeister, S., Wilson, T. L., et al. 1997, A&AS, 126, 197  
Dieter, N. H., & Ewen, H. I. 1964, Nature, 201, 279  
Dobler, G., Finkbeiner, D. P., Cholis, I., Slatyer, T., & Weiner, N. 2010, ApJ, 717, 825  
Espinoza, P., Selman, F. J. & Melnick, J. 2009, ApJ, 504, 563  
Figer, D. F., McLean, I. S., & Morris, M. 1999, ApJ, 514, 202  
Friedli, D. & Martinet, L. 1993, A&A, 277, 27

- Geballe, T. R., & Oka, T. 1996, *Nature*, 384, 334
- Geballe, T. R., McCall, B. J., Hinkle, K. H., & Oka, T. 1999, *ApJ*, 510, 251
- Geballe, T. R., & Oka, T. 2010, *ApJ*, 709, L70
- Geballe, T. R., Lambrides, E., Schlegelmilch, B., Yeh, S. C. C., Goto, M., Westrick, C., Oka, T., & Najarro, F. 2019a, *ApJ*, 872, 103
- Geballe, T. R., Oka, T., & Goto, M. 2019b, *Phil. Trans. R. Soc. Lond. A* 377, 2018-0400
- Genzel, R., & Townes, C. H. 1987, *ARA&A*, 25, 377
- Goldreich, P., & Kwan, J. 1974, *ApJ*, 189, 441
- Goldstein, Jr., S. J., Gundermann, E. J., Penzias, A. A., & Lilley, E. E., 1964, *Nature*, 203, 65
- Goto, M., McCall, B. J., Geballe, T. R., Usuda, T., Kobayashi, N., Terada, H., & Oka, T., 2002, *PASJ*, 54, 951
- Goto, M., Usuda, T., Nagata, T., Geballe, T. R., McCall, B. J., Indriolo, N., Suto, H., Henning, T., Morong, C. P., & Oka, T. 2008, *ApJ*, 688, 306
- Goto, M., Usuda, T., Geballe, T. R., Indriolo, N., McCall, B. J., Henning, T., Oka, T., 2011, *PASJ*, 63, L13
- Goto, M., Geballe, T. R., Indriolo, N., Yusef-Zadeh, F., Usuda, T., Henning, T., & Oka, T. 2014, *ApJ*, 786, 96
- Güsten, R., & Downes, D. 1981, *A&A*, 99, 27
- Heays, A. N., Bosman, A. D., & van Dishoeck, E. F. 2017, *A&A*, 62, A105
- Heiligman, G. M. 1987, *ApJ*, 314, 747
- Henshaw, J. D., Longmore, S. N., Kruijssen, J. M. D., et al. 2016, *MNRAS*, 457, 2675
- Heywood, I., Camilo, F., Cotton, W. D., et al. 2019, *Nature*, 573, 235
- Indriolo, N., Geballe, T. R., Oka, T., & McCall, B. J. 2007, *ApJ*, 671, 1736
- Indriolo, N., & McCall, B. J. 2012, *ApJ*, 745, 91
- Kaifu, N., Kato, T., & Iguchi, T. 1972, *Nature*, 238, 105
- Kaifu, N., Iguchi, T., & Kato, T. 1974, *PASJ*, 26, 117
- Kataoka, J., Sofue, Y., Inoue, Y., Akita, M., Nakashima, S., & Totani, T. 2018, *Galaxies*, 6, 27
- Kobayashi, Y., Okuda, H., Sato, S., Jugaku, J., & Dyck, H. M. 1983, *PASJ*, 35, 101
- Kormendy, J., & Kennicutt, Jr., R. C. 2004, *ARA&A*, 42, 603
- Koyama, K., Awaki, H., Kunieda, H., Takano, S., Tawara, Y., Yamauchi, S., Hatsukade, I., & Nagase, F. 1989, *Nature*, 339, 603
- Kruijssen, J. M. D., Dale, J. E., & Longmore, S. N. 2015, *MNRAS*, 447, 1059
- Langer, W. D., Goldsmith, P. F., Pineda, J. L., et al. 2015, *A&A* 576, A1
- Law, C. J., Backer, D., Yusef-Zadeh, F., & Maddelena, R. 2009, *ApJ*, 695, 1070
- Lazio, T. J. W., & Cordes, J. M. 1998, *ApJ*, 505, 715
- Lindblad, B. 1927, *MNRAS*, 87, 553
- Lindsay, C. M., & McCall, B. J. 2001, *JMoSp*, 210, 60
- Linke, R. A., Stark, A. A., & Frerking, M. A. 1981, *ApJ*, 243, 147
- Liszt, H. S. 1992, *ApJS*, 82, 495
- Liszt, H. S., & Burton, W. 1978, *ApJ*, 226, 790
- Liszt, H. S., & Burton, W. 1980, *ApJ*, 236, 779
- Martin, C. I., Walsh, W. M., Xiao, K., Lane, A. P., Walker, C. K., & Stark, A. A. 2004, *ApJS*, 150, 239
- McCall, B. J., Geballe, T. R., Hinkle, K. H., & Oka, T. 1998, *Science*, 279, 1910
- McCall, B. J., Geballe, T. R., Hinkle, K. H., & Oka, T. 1999, *ApJ*, 522, 338
- McCall, B. J., Huneycutt, A. J., Saykally, R. J., et al. 2003, *Nature*, 422, 500
- McCall, B. J., Huneycutt, A. J., & Saykally, R. J. et al. 2004, *PhRv*, 70, 052716
- McCammon, D., Burrows, D. N., Sanders, W. T., & Karushaar, W. L. 1983, *ApJ*, 269, 107
- McCammon, D., & Sanders, W. T. 1990, *ARA&A*, 28, 657
- McGee, R. X. 1970, *AuJPh*, 23, 541
- Menon, T. K., & Ciotti, J. E. 1970, *Nature*, 227, 579
- Miller, S., Tennyson, J., Geballe, T. R., & Stallard, T. 2020, *Rev. Mod. Phys.*, 92.1
- Mizus, I. I., Alijah, A., Zobov, N. F., Lodi, L., Kyuberis, A. A., Yurchenko, S. N., Tennyson, J., & Polyansky, O. L. 2017, *MNRAS*, 468, 1717
- Molinari, S., Bally, J., Noriega-Crespo, A., et al. 2011, *ApJ*, 735, L33
- Möllenhoff., C. 1976, *A&A*, 50, 105
- Morris, M., & Serabyn, E. 1996, *ARA&A*, 34, 645
- Nagata, T., Woodward, C. E., Shure, M., Pipher, J. L., & Okuda, H. 1990, *ApJ*, 351, 83
- Nagata, T., Hyland, A. R., Straw, S. M., Sato, S., & Kawara, K. 1993, *ApJ*, 406, 501
- Neale, L., Miller, S., & Tennyson, J. 1996, *ApJ*, 464, 516
- Oka, T., 1970, *ApJ*, 160, L69
- Oka, T., 1980, *PhRvL*, 45, 531
- Oka, T. 2013, *ChRv*, 113, 8738 B. 1978, *ApJ*, 226, 790
- Oka, T., & Epp, E. 2004, *ApJ*, 613, 349
- Oka, T., Geballe, T. R., Goto, M., Usuda, T., & McCall, B. J. 2005, *ApJ*, 632, 882
- Oka, T., Geballe, T. R., Goto, M., Usuda, T., McCall, B. J., & Indriolo, N. 2019, *ApJ*, 883, 54 (Paper I)
- Oka, T., Shimizu, F. O., Shimizu, T., & Watson, J. K. G. 1971, *ApJ*, 156, L15
- Oka, T., Hasegawa, T., Hayashi, M., Handa, T., Sakamoto, S. 1998a, *ApJ*, 493, 730
- Oka, T., Hasegawa, T., Sato, F., Tsuboi, M., Miyazaki, A. 1998b, *ApJS*, 118, 455

- Oka, T., Onodera, Y., Nagai, M., Tanaka, K., Matsumura, S., & Kamegai, K. 2012, *ApJS*, 201, 14
- Okuda, H., Shibai, H., Nakagawa, T., Matsuhara, H., & Kobayashi, Y., Kaifu, N., Nagata, T., Gatley, I., & Geballe, T. R. 1990, *ApJ*, 351, 89
- Oort, J. H. 1977, *ARA&A*, 15, 295
- Pan, F.-S., & Oka, T. 1986, *ApJ*, 305, 518
- Ramírez, S. V., Arendt, R. G., Sellgren, K., et al. 2008, *ApJS*, 175, 147
- Regan, M. W., Sheth, K., Vogel, S. N. 1999, *ApJ*, 526, 97
- Ridley, M. G. L., Sormani, M. C., Tre, R. G., Magorrian, J., & Klessen, R. S. 2017, *MNRAS*, 469, 2251
- Robinson, B. J., Gardner, F. F., van Damme, K. J., & Bolton, J. G. 1964, *Nature*, 202, 989
- Robinson, B. J. & McGee, R. X. 1970, *AuJPh*, 23, 405
- Rodríguez-Fernandez, N. J., Martín-Pintado, J., Fuente, A., & Wilson, T. L., 2004, *A&A*, 427, 217
- Rodríguez-Fernandez, N. J., Combes, F., Martín-Pintado, J., Wilson, T. L., & Apponi, A., 2006, *A&A*, 455, 963
- Rougoor, G. W., & Oort, J. H. 1960, *PNAS*, 46, 1
- Rougoor, G. W. 1964, *BAN*, 17, 38
- Sakashita, S. 1971, *Ap&SS*, 14, 431
- Sawada, T., Hasegawa, T., Handa, T. et al. 2001, *ApJS*, 136, 189
- Sawada, T., Hasegawa, T., Handa, T., Cohen, R. J. 2004, *MNRAS*, 349, 1167
- Schneider, F. R. N., Izzard, R. G., De Mink, S. E., et al. 2014, *ApJ*, 780, 117
- Scoville, N. Z., 1972, *ApJ*, 175, L127
- Scoville, N. Z., Solomon, P. M., & Thaddeus, P. 1972, *ApJ*, 172, 335
- Scoville, N. Z., & Solomon, P. M. 1974, *ApJ*, 187, L67
- Snowden, S. L., Egger, R., Freyberg, M. J., et al. 1997, *ApJ*, 485, 125
- Sofue, Y. 1973, *PASJ*, 25, 207
- Sofue, Y. 1976, *PASJ*, 28, 19
- Sofue, Y. 1977, *A&A*60, 327
- Sofue, Y. 1994, *ApJ*, 431, L91
- Sofue, Y. 1995a, *PASJ*, 47, 527
- Sofue, Y. 1995b, *PASJ*, 47, 551
- Sofue, Y. 2000, *ApJ*, 540, 224
- Sofue, Y. 2006, *PASJ*, 58, 335
- Sofue, Y. 2013, *PASJ*, 65, 118
- Sofue, Y. 2017, *MNRAS*, 470, 1982
- Sofue, Y. 2019, *MNRAS*, 484, 2954
- Sofue, Y., & Handa, T., 1984, *Nature*, 310, 568
- Sormani, M. C., Binney, J., & Magorrian, J. 2015a, *MNRAS*, 449, 2421
- Sormani, M. C., Binney, J., & Magorrian, J. 2015b, *MNRAS*, 451, 3437
- Sormani, M. C., Binney, J., & Magorrian, J. 2015c, *MNRAS*, 454, 1818
- Su, M., Slatyer, T. R., & Finkbeiner, D. P. 2010, *ApJ*, 724, 1044
- Suzuki, T. K., Fukui, Y., Torii, K., Machida, M., & Matsumoto, R. 2015, *MNRAS*, 454, 3049
- Townes, C. H., & Cheung, A. C. 1969, *ApJ*, 157, L103
- Tsujimoto, S., Oka, T., Takekawa, S., Yamada, M., Tokuyama, S., Iwata, Y., & Roll, J. A. 2018, *ApJ*, 856, 91
- Uchida, Y. 1970, *PASJ*, 22, 341
- van der Kruit, P. C. 1970, *A&A*, 4, 462
- van Dishoeck, E. F. 1988, in *Rate coefficients in astrochemistry*, eds. T. J. Millar, & D. A. Williams (Dordrecht: Kluwer Academic Publishers), 49
- Viehmann, T., Eckart, A., Schödel R., Moulata, J., Straubmeier, C., & Pott, J.-U. 2005, *A&A*433, 117
- Weinreb, S., Barrett, A. H., Meeks, L. M., & Henry, J. C. 1963, *Nature*, 200, 829
- Whiteoak, J. B. 1994, *AuJPh*, 47, 577
- Yusef-Zadeh, F., & Wardle, M. 2019, *MNRAS*, 490, L1
- Yusef-Zadeh, F., Wardle, M., Heywood, I., Cotton, M., & Royster, M. 2019, *arXiv*, 1912, 11057
- Zubovas, K., Wynn, G. A., & Gualandris, A. 2013, *ApJ*, 771, 118